Characterisation of elastic turbulence in a serpentine micro-channel

Antoine Soulies, Julien Aubril, Cathy Castelain, Teodor Burghelea

Characterisation of elastic turbulence in a serpentine micro-channel

Antoine Souliès,[a] Julien Aubril,[b] Cathy Castelain,[c] and Teodor Burghelea[d]
Université de Nantes, CNRS, Laboratoire de Thermique et Energie, UMR 6607, La Chantrerie, Rue Christian Pauc, B.P. 50609, F-44306 Nantes Cedex 3, France

(Received 9 March 2017; accepted 14 July 2017; published online 2 August 2017)

A systematic experimental investigation of the onset, development, and statistical and scaling properties of elastic turbulence in a curvilinear micro-channel of a dilute solution of a high molecular weight polymer is presented. By measurements of time series of high spatial resolution flow fields performed over a time 320 times longer than the average relaxation, we show that the transition to elastic turbulence occurs via an imperfect bifurcation. Slightly above the onset of the primary elastic instability, rare events manifested through a local deceleration of the flow are observed. By measurements of the spatial distributions and statistics of the second invariant of the rate of strain tensor, we show that the main prediction of the theory regarding the saturation of root mean square of fluctuations of the velocity gradients is qualitatively verified though a quantitative agreement could not be found. A systematic analysis of the statistics of the fluctuations of flow fields in terms of spatial and temporal correlations, power spectra, and probability distributions is presented. The scaling properties of structure functions of the increments of the velocity gradients are discussed. Our experimental findings call for further developments of the theory of elastic turbulence in bounded flow channels. *Published by AIP Publishing.* [http://dx.doi.org/10.1063/1.4996356]

I. INTRODUCTION

The addition of a tiny amount of high molar mass linear polymer molecules to a fluid makes it elastic and capable of storing stresses that depend on the flow history.[6] The polymer contribution to the stress tensor depends on the flow forcing in a strongly nonlinear fashion and may lead to a loss of the hydrodynamic stability of shear flows with curvilinear trajectories.[27,33,38] The purely elastic instabilities are triggered in the absence of any inertial contributions (i.e., at vanishingly small Reynolds numbers, *Re*) when the elastic energy overcomes the dissipation due to polymer relaxation. The ratio of the nonlinear elastic term to the linear relaxation one is defined by the Weissenberg number *Wi*, which is the main control parameter, and the purely elastic instabilities in curvilinear shear flows are observed when $Wi > Wi_c$. A further increase of *Wi* past the onset of the primary elastic instability leads to the observation of the so-called "*elastic turbulence*."[21] The elastic turbulence is a random flow state solely driven by the nonlinear elastic stresses and, as opposed to its inertial counterpart, it can be observed at arbitrarily small Re. Following the discovery of elastic turbulence, a number of experimental studies have revealed several of its key features in various flow macroscopic configurations.[10,12–14] Although the most dramatic effect of elastic turbulence manifested through a fully developed chaotic flow capable of efficiently mixing low diffusivity tracers was observed in a curvilinear microscopic flow,[8,9] a full spatial and temporal characterisation of such microscopic channel flows in a wide range of *Wi* numbers is, to the best of our knowledge, still unavailable in the literature. Below we summarise several of the main features of elastic turbulence mainly observed in either closed or open macroscopic flows with curved streamlines.

The transition to elastic turbulence is accompanied by a sharp growth of the flow resistance.[8,14,21] The elastic turbulent flow fields are spatially smooth (meaning that the second-order spatial derivative of the velocity field is roughly an order of magnitude smaller than the first one) and their dominant space scale is set by the size of the fluid container *W*.[12,14] Thus, the elastic turbulent flow field may be considered locally linear (i.e., locally uniform rate of strain). Consequently, the spectra of the velocity fluctuations decay algebraically $P \propto f^{-\delta}$ with $\delta \approx 3.5$.[7,14,21,28]

The elastic turbulent flows are characterised by divergent Lagrangian trajectories and, consequently, positive finite time Lyapunov exponents (FTLE) could be measured by both numerical integration of the measured velocity fields and by direct tracking of tracer particles in the flow.[10] The elastic turbulent flows are highly correlated over space, and the characteristic correlation distance is comparable to the size of the fluid container.[12] Systematic experiments performed in a macroscopic von Karman swirling flow between disks by means of both Laser Doppler Velocimetry (LDV) and Digital Particle Image Velocimetry (DPIV)[14] revealed a new characteristic space scale of elastic turbulence: the width of the stress boundary layer. The Eulerian temporal auto-correlation functions decay rather fast with characteristic correlation times comparable to the longest polymer relaxation time.[14]

From a practical perspective, it has been demonstrated experimentally that elastic turbulent flows are able to mix

[a] Antoine.Soulies@univ-nantes.fr
[b] Julien.Aubril@univ-nantes.fr
[c] Cathy.Castelain@univ-nantes.fr
[d] Author to whom correspondence should be addressed: Teodor.Burghelea@univ-nantes.fr

efficiently very viscous fluids in both macroscopic open channels[22] and micro-channels.[8,9] Moreover, the elastic turbulent flows are an ideal realization of the Batchelor regime of mixing. More recently but equally important from a practical perspective, it has been shown that elastic turbulent flows transfer heat up to four times more efficiently than purely conductive laminar flows.[42] From a theoretical standpoint, elastic turbulence remains, in our opinion, an insufficiently explored area and, according to Ref. 39, understanding elastic turbulence might be a fundamental step towards understanding the long standing problem of drag reduction.

The only existing theory of elastic turbulence in dilute solutions of polymers with linear elasticity has been published shortly after its discovery by Balkovsky, Fouxon, and Lebedev.[2] A central goal of the theory was to explain the experimentally observed algebraic decay of the spectra of the velocity fluctuations.

As already noted through the Introduction, the bulk of the existing experimental studies of elastic turbulence have been performed in a macroscopic von Karman swirling flow and fewer results are available for channel flows. A systematic investigation of elastic turbulence in a millimetre size serpentine channel aiming to probe several of the key predictions of the theory of elastic turbulence has been recently performed by Jun and Steinberg.[25] Their work provides a detailed description of the transition to elastic turbulence and of its dynamics in a broad range of Weissenberg numbers. A systematic description of the elastic stress boundary layer and of its scaling properties is provided. Contrary to the theoretical prediction and the previous experimental results obtained in a macroscopic von Karman flow[14] concerning the saturation of the elastic stresses assessed via the level fluctuations of the velocity gradients in the bulk of the flow, they found a monotone increase with the Weissenberg number.

A systematic experimental characterisation of elastic turbulence in a curvilinear micro-channel is, to the best of our knowledge, still missing, and this sets the general goal of the present contribution. The motivation of focusing on a curvilinear microscopic flow is three-fold. From a fundamental standpoint, we are interested in understanding the role of spatial confinement on the dynamics of elastic turbulence (and check if the main features observed in macroscopic flows are preserved). From a practical perspective, such flows have already proved their ability to mix efficiently and further practical applications could be found in efficiently transporting heat at micro-scale and enhancing chemical reactions in a lab on a chip environment. Lastly, as compared with their macroscopic counterpart, the microscopic channel flows allow measurements of flow speeds and velocity gradients with both very high spatial and temporal resolution.

Several particular goals of the paper can be listed as follows:

i. Provide an experimental description of the transition to elastic turbulence in a curvilinear micro-channel and identify its nature.
ii. Provide a systematic description of spatial structure of the flow around both the transitional zone and the fully developed elastic turbulent regime with a particular focus on both the time averaged flow components and their corresponding fields of fluctuations.
iii. Measure the spatial distributions of the velocity gradients and their fluctuations.
iv. Describe the spatial and temporal correlations of each flow component as a function of the Weissenberg number.
v. Describe the statistics of several relevant hydrodynamic quantities such as velocity fluctuations, flow accelerations, spatial increments of the velocity gradients and describe the scaling of the structure functions in a wide range of Weissenberg numbers.
vi. Compare the results obtained with the previous experimental results and assess the validity of the main assumptions and predictions of the theory of elastic turbulence.

The paper is organized as follows. A brief reminder of the theory of elastic turbulence is presented in Sec. II. The experimental methods are presented in Sec. III. A particular attention has been devoted to the rheological characterisation of the fluids in Sec. III D and to the validation of the flow investigation technique in Sec. III E. The experimental results are presented in Sec. IV according to the sequence of goals listed above. The paper closes with a summary of the main conclusions and a discussion of several remaining open questions, Sec. V.

II. HYDRODYNAMIC THEORY OF ELASTIC TURBULENCE

The theory of elastic turbulence of a dilute solution of polymers with linear elasticity and the feedback reaction on the flow was developed by Lebedev *et al.*[2,19] The distinctive property of solutions of high molar mass linear polymers is the dependence of the stresses on the flow history.[6] Thus, once the flow forcing is removed, the stress decays with a macroscopic relaxation time λ (quite often as large as tens of seconds) rather than instantly vanishing. By noting that for a dilute solution the total stress tensor can be decomposed into a solvent and a polymer contribution $\boldsymbol{\tau} = \boldsymbol{\tau}_s + \boldsymbol{\tau}_p$, the equation of motion takes the form

$$\frac{\partial \vec{V}}{\partial t} + \left(\vec{V}\,\nabla\right)\vec{V} = -\frac{\nabla p}{\rho} + \frac{\eta_s}{\rho}\Delta\vec{V} + \frac{\nabla\,\boldsymbol{\tau}_p}{\rho}. \tag{1}$$

The mathematically simplest model accounting for the evolution of the polymer contribution to the stress tensor in a flow is a single mode Maxwell type constitutive relation

$$\boldsymbol{\tau}_p + \lambda\frac{D\boldsymbol{\tau}_p}{Dt} = \eta_p\left[\nabla\vec{V} + \left(\nabla\vec{V}\right)^T\right]. \tag{2}$$

Here $D\boldsymbol{\tau}_p/Dt$ stands for the material time derivative and $\eta_p = \eta - \eta_s$ is the polymer contribution to the solution viscosity. A commonly used definition of the material time derivative is the upper convective time derivative

$$\frac{D\boldsymbol{\tau}_p}{Dt} = \frac{\partial\boldsymbol{\tau}_p}{\partial t} + \left(\vec{V}\cdot\nabla\right)\boldsymbol{\tau}_p - \left(\vec{V}\cdot\nabla\right)\cdot\boldsymbol{\tau_p} - \boldsymbol{\tau_p}\cdot\left(\vec{V}\cdot\nabla\right)^T. \tag{3}$$

The nonlinear terms in the right hand side of Eq. (3) account for the translation, rotation, and stretching of fluid elements and are all of the order of $\lambda\frac{V}{L}\tau_p$.

Equations (2) and (3) are referred to as the Oldroyd-B rheological model for polymer solutions.[6]

A key ingredient of the theory of elastic turbulence is to relate the dynamics of the elastic stress tensor $\boldsymbol{\tau}_p$ to the dynamics of a vector field with a linear damping.[2,15,19,34] This can be done by noting that if one neglects the thermal fluctuations, the elastic stress tensor is uniaxial, $\tau_p^{i,j} = B_iB_j$, which allows one to derive an equation similar to the equation for the magnetic field in magnetohydrodynamics (MHD),

$$\frac{\partial\vec{B}}{\partial t} + \left(\vec{V}\,\nabla\right)\vec{B} = \left(\vec{B}\,\nabla\right)\vec{V} - \frac{\vec{B}}{\lambda}, \tag{4}$$

$$\nabla\cdot\vec{B} = 0. \tag{5}$$

The stretching of the magnetic field lines is similar to the stretching of polymer molecules in the flow, and the sole difference with respect to the MHD case comes from the linear relaxation term $\frac{\vec{B}}{\lambda}$, which replaces the diffusion term. In the absence of inertial contributions, $Re << 1$, the momentum conservation equation can be written as

$$\nabla P = \rho\left(\vec{B}\nabla\right)\vec{B} + \eta_s\Delta\vec{V}, \tag{6}$$

$$\nabla\cdot\vec{V} = 0. \tag{7}$$

In the absence of significant inertial contributions ($Re \ll 1$), which is the case for elastic turbulence, the kinetic energy of the polymer solution can be neglected in comparison with the elastic one. The dissipation of the elastic energy is, however, due to both viscous dissipation due to the solvent viscosity and polymer relaxation,

$$\frac{d}{dt}\int d\vec{r}\frac{B^2}{2} = -\frac{1}{\lambda}\int d\vec{r}\frac{B^2}{2} - \frac{\eta_s}{\rho}\int d\vec{r}\left(\nabla_j V_i\right)^2. \tag{8}$$

With the appropriate boundary conditions, Eqs. (4) and (6) exhibit an elastic instability at $Wi = Wi_c$, where $Wi = \lambda\dot{\underline{\underline{\gamma}}}$ and the instability results in a chaotic and statistically stationary dynamics. Here $\dot{\underline{\underline{\gamma}}}$ is the second invariant of the rate of strain tensor.

The theory of elastic turbulence in an unbounded flow of a polymer solution is built upon two central assumptions as follows:

1. The local feedback of the stretched polymer molecules on the flow field leads to a statistically stationary state characterised by the saturation of both the polymer contribution to the stress tensor τ_p and the root mean square (rms) of the fluctuations of the velocity gradients $\left(\frac{\partial V_i}{\partial x_j}\right)^{rms}$. Consequently, corresponding to a fully developed elastic turbulent regime, the local Weissenberg number defined as $Wi_{loc} = \lambda\left(\frac{\partial V_i}{\partial x_j}\right)^{rms}$ saturates and, in the bulk of the flow, its saturation value is $Wi_{loc} \approx 1$.
2. Both dissipative terms due to viscosity and polymer relaxation that appear in the equation for the dissipation of elastic energy are of the same order of magnitude $\frac{\tau_p}{\lambda} \approx \frac{\eta}{\rho}\left(\nabla\vec{V}\right)^2$ or, equivalently, $\frac{\tau_p\lambda\rho}{\eta} \approx Wi_{loc}^2$.

According to Ref. 2, the first assumption may be phenomenologically understood in the context of a strong back reaction of the extended polymer molecules to the flow as follows. If the instantaneous velocity gradients exceed the reciprocal relaxation time $1/\lambda$, the polymer coils are stretched, which results in an increase of the elastic stresses that damps the velocity gradients. Conversely, if the velocity gradients are much smaller than $1/\lambda$, the polymer molecules retract and produce no feedback to the flow. Thus, the velocity gradients tend to increase to the characteristic value corresponding to the pure solvent, which is significantly larger than $1/\lambda$ above the onset of the transition. The second assumption is consistent with the saturation of the elastic stresses far above the onset of the primary elastic instability.

Next, if one denotes by $\vec{V}'$ and $\vec{B}'$ the small scale fluctuating parts of the fields $\vec{V}$ and $\vec{B}$, it can be shown that the Fourier components satisfy the linear relationship

$$\vec{V}' = \frac{i\rho\left(\vec{k}\cdot\vec{B}\right)}{\eta k^2}\vec{B}'. \tag{9}$$

Here $\vec{k}$ is the wave number and i is the imaginary unit. Equation (9) allows one to show that the spherically normalised spectra of fluctuations of $\vec{V}'$ and $\vec{B}$ denoted by $E(k)$ and $F(k)$, respectively, satisfy the following relationships:[19]

$$E(k) \propto V^2L(kL)^{-\delta}, \tag{10}$$

$$F(k) \propto B^2L(kL)^{2-\delta}. \tag{11}$$

With the assumptions $\nabla V' \ll \nabla V$ and $B' \ll B$, it can be shown that $\delta > 3$.[19] The algebraic decay of the velocity spectrum has been measured by means of *LDV* measurements (and using Taylor's frozen flow hypothesis, it was converted from the frequency domain to the wave number domain) in a macroscopic von Karman flow and, subsequently, in a macroscopic serpentine channel by Groisman and Steinberg in Refs. 21 and 22. Direct measurements of the spectra in the spatial domain by means of DPIV revealed a decay exponent $\delta \approx 3.5$.[7,14] Contrary to the case of the inertial turbulence, the algebraic scalings of the kinetic and elastic energies are not related to a cascade of energy (or other conserved physical quantities). Because the velocity spectrum decays faster than k^{-3}, the dominant space scale is set by the size of the fluid container L, and the velocity fluctuations are strongly correlated over distances comparable to L. This has been probed experimentally by measurements of the space-time correlation surface in a macroscopic von Karman swirling flow configuration.[12]

A k^{-1} like decay of the spectrum of the fluctuations is characteristic for the decay of a passive scalar in a smooth random flow field in the so-called Batchelor regime of mixing.[4] Such algebraic decay has been observed for the mixing of a fluorescent tracer by an elastic turbulent flow in both microscopic[7–9] and macroscopic channel flows.[24] More recently and somehow unexpectedly, a similar spectral decay has been observed for the fluctuations of the temperature in an elastic turbulent von Karman swirling flow cooled from below.[42] This indicates that, in spite of the strong temperature dependence of the rheological properties (notably the relaxation time and the shear viscosity), the temperature field behaves like a passive

scalar. Thus, if the decay exponent of the velocity spectrum is $\delta \approx 3$, Eq. (11) suggests that the stress is passively advected by the large scale chaotic smooth flow in a regime of elastic turbulence.

Although many fundamental features of elastic turbulent flows (such as flow smoothness, the algebraic decay of spectra of fluctuations, and the decay of the flow correlation) have been investigated experimentally in various macroscopic flows (Couette flow between rotating cylinders, von Karman swirling flow, and curvilinear channel flow), the main assumption of the theory concerning the saturation of velocity gradients still awaits a systematic experimental test.

III. EXPERIMENTAL METHODS

A. Micro-channel design, microscopic flow control, and data acquisition protocol

The experiments have been performed with a serpentine micro-channel schematically illustrated in Fig. 1(a). It consists of $N = 200$ smoothly interconnected half circular rings with the inner radius $R_1 = 50\,\mu m$ and the outer radius $R_2 = 250\,\mu m$. A magnified view of a circular half-ring is presented in the top inset of Fig. 1(a). The width of the micro-channel is $W = R_2 - R_1 = 200\,\mu m$ and its depth is $H = 200\,\mu m$. The geometric aspect ratio relevant to the onset of the primary elastic instability[31,46] is $\alpha = R_1/W = 0.25$.

The micro-channel was machined in an aluminium block with the dimensions 6 cm × 3 cm × 0.4 cm using a fast spinning (14 000 rot/min) micro-milling head (Nakanishi, model *HES*510–*BT*40) mounted on a commercial computer controlled milling machine (Twinhorn, model *VH*1010). By a precise alignment of the initial aluminium block on the stage of the milling machine, the depths of the micro-channel were uniform over its entire lengths with an end to end variation (measured by means of optical profilometry) smaller than one percent. The average roughness of the edges of the micro-channel as resulted from the micro-milling process is roughly of the order of a micron that accounts for half percent of the channel width. We note that this level of edge smoothness is comparable to that obtained via the classical micro-lithography techniques. The micro-channel was sealed with a strong and optically transparent adhesive tape (3*M*, model 727–1280). The micro-channel chip is mounted on an inverted epifluorescent microscope (Nikon Eclipse *TS*–100) schematically illustrated in Fig. 1(b). The microscopic flows are generated and controlled by the difference in hydrostatic pressure between the inlet and outlet fluid containers. This is achieved by rigidly mounting the inlet fluid container on a vertical translational stage driven by a precise stepping motor (Isel, Germany). The position of the stage is controlled within 1 μm accuracy.

The light emitted by the *LED* panel *LP* is directed via the excitation filter *EXF* (band pass, 450–490 nm) to the microscope objective *MO* (T Plan SLWD *X*20). Alternatively, in order to get a larger view of the flow structure, we have used a *X*10 microscope objective. The flow was seeded with an amount of 150 ppm fluorescent particles with a diameter of 0.9 μm (Fluoresbrite Multifluorescent from Polysciences) and the flow images were recorded by a digital camera (GigE Vision—compliant Prosilica GE680C from Allied Vision.). In order to avoid the transient states, after setting the pressure drop we have waited for 10 s before starting the image acquisition process. The camera is connected to a personal computer running on Windows 7 (64 bits) via a dedicated Ethernet PCI card (Intel Pro 1000). To extend the capabilities of the data transmission, high performance National Instruments drivers are preferred rather than Intel ones. The image acquisition software was developed in house under LabVIEW 2015 64 bits. The 64 bits version has been deliberately used in order to extend the memory usage allowing the images to be stored in the RAM. Other commercial software tools require a high performance *CPU* for online data processing as well as *SSD* hard drives online saving and lower computer resources render these tools unreliable. Using the *RAM* for the temporary data

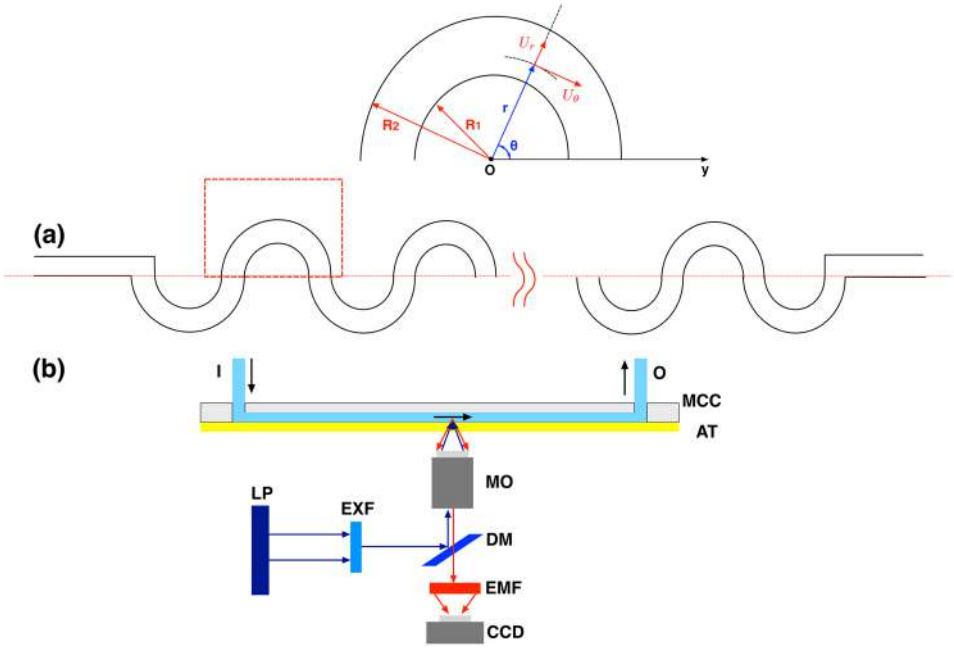

FIG. 1. (a) Schematic view of the serpentine micro-channel. The top inset presents a magnified view of the curvilinear element of the micro-channel together with the coordinate system. (b) Schematic view of the experimental setup (not in scale): MCC—micro-channel chip, I—micro-channel inlet, O—micro-channel outlet, AT—adhesive tape, MO—microscope objective, DM—dichroic mirror, LP—light emitting diode (LED), EXF—excitation filter, EMF—emission filter, CCD—digital camera.

storage, however, limits the total number of images that can be acquired. To be able to acquire images over times significantly longer than the polymer relaxation time, a special data acquisition protocol has been used according to which pairs of images separated by a time t_1 have been acquired at equal time intervals $t_2 > t_1$. The inter-frame t_1 has been adjusted from 20 ms to 300 ms depending on the value of the driving pressure. This adaptive inter-frame technique allowed one to maintain the average displacement of individual flow tracers within the range 5–20 pixels, which is a pre-condition for a reliable velocity measurement. The instrumental error of the flow field measurements was smaller than 5%, see Secs. III B and III E for a full description. The time interval between subsequent pairs of images was $t_2 = 0.5$ s. A special attention was paid to insure an accurate timing during the image acquisition process. First, a hardware-timed digital output pattern is used to trig the camera using a NI USB 6343 multifunction acquisition card controlled by NI-DAQmx drivers. Because the card is coded to run as standalone, the computer downturns cannot affect the triggering. Second, each image is written together with its own hardware (camera) timestamp, ensuring that both t_1 and t_2 are accurately measured. Another issue that had to be addressed was to synchronize the image acquisition with flow driving. For this purpose, the position of the vertical translational stage carrying the inlet fluid container was controlled and synchronized with the image acquisition process via an ISEL 116 Flash controller integrated within the same LabVIEW interface. A full experimental campaign consisted of measurements performed during an increasing/decreasing ramp of the driving pressures Δp at the same position half-way downstream and in the middle plane of the micro-channel. Each branch of the flow ramp consisted of 27 values of the driving pressures judiciously chosen in order to span the laminar, transitional, and fully developed elastic turbulent regimes. Corresponding to each point of the ramp, images have been acquired during 1200 s.

B. Data analysis

The main tool used to systematically investigate the spatial and temporal features of the flow was an adaptive multi-grid Digital Particle Image Velocimetry (DPIV) (see Refs. 35 and 36 for a detailed description of the method) entirely developed in house under MATLAB (together with the "Image Processing Toolbox"), which followed the steps briefly described below. First, a background was calculated by averaging all the images of the first time series we have acquired. Second, the average background was subtracted from images. Third, the pixel resolution has been artificially increased by a factor of 1.5^2 by a re-gridding procedure based on a bicubic interpolation algorithm. This allows one to artificially increase the density of tracers, which ultimately translates into an improved spatial resolution of the velocity fields down to 1.8 μm. Fourth, the contrast of the images obtained from the previous step has been augmented using an adaptive histogram technique. Finally, pairs of pre-processed images separated in time by the inter-frame t_1 are passed to a multi-pass *DPIV* algorithm using a sequence of squared interrogation windows with sizes [128,64,32,16,8].

C. Preparation and physical properties of the polymer solution

A 80 ppm anionic polyacrylamide (*PAAM*) solution with the molecular weight $M_w = 22{\cdot}10^6$ Da has been used as a working fluid. The solvent was a 65 wt. % aqueous solution of sucrose. The anhydrous sucrose was not of an analytical grade (pure) but simply a commercially available sugar (Sucre Crystal from Béghin Say, France). The viscosity of the Newtonian solvent was $\eta_s = 162$ mPa · s (at the room temperature $T_0 = 20\,^{\circ}$C), which ensures large characteristic relaxation times of the polymer solution. The polymer solutions were prepared according to the following protocol. First we dissolved 0.9 g of anhydrous *PAAM* and 3 g of NaCl into 275 ml of deionised water by gentle shaking. NaCl was added to fix the ionic contents within the polymer solution. Next the solution was mixed for 3 h in a commercial mixer with a propeller at a moderate speed. The rationale for this step is to cause a controlled mechanical degradation of the longest *PAAM* molecules in order to cut the tail of the molecular weight distribution of the broadly dispersed *PAAM* sample. In a solution with a broad distribution of polymer molecular weights, the heaviest molecules, which are most vulnerable to mechanical degradation, bring the major contribution to the solution elasticity, but may break in the course of the experiment. This may result in inconsistencies of the experimental results. Finally, 9 g of isopropanol was added to the solution to prevent it from ageing and water was added up to 300 g. The final concentrations of *PAAM*, NaCl, and isopropanol in the stock solution were 3000 ppm, 1%, and 3%, respectively. This master solution was used to prepare 80 ppm *PAAM* solution in a Newtonian solvent. To prevent the bacterial growth and allow the storage over extended periods of time, we have finally added to the polymer solutions an amount of 250 ppm of sodium azide (NaN_3). The density of the polymer solution was measured at room temperature by accurately weighting fixed volumes of fluid, $\rho = 1300$ kgm^{-3}.

The intrinsic viscosity of the solution defined as $[\eta] = \lim_{c\to 0} \frac{\eta-\eta_s}{c\eta_s}$ can be estimated using the Mark-Houwink relation as $[\eta] = 6.31 \cdot 10^{-3} M_w^{3\nu-1}$.[26,43] Here the exponent ν characterizes the scaling of the equilibrium radius of gyration of the polymer chain $R_g \propto M_w^{\nu}$, and for a good solvent, $\nu = 0.6$. For $M_w = 22 \cdot 10^6$ Da, one obtains $[\eta] \approx 4720$ ml/g. The overlap concentration defined as the critical concentration at which the polymer coils start to overlap may be estimated as $c^* = 1/[\eta]$, which gives $c^* \approx 211$ ppm by weight. This value is in fair agreement with the value given in Ref. 37, $c^* \approx 180$ ppm. According to Doi and Edwards,[16] the gyration radius of the polymer coils may be calculated as $R_g \approx \left(\frac{3M_w}{4\pi N_A c^*}\right)^{1/3} \approx 0.345$ μm. Here N_A stands for Avogadro's number. Within the framework of the Zimm model,[47] the longest relaxation time of a polymer chain in a good solvent can be approximated by:

$$\lambda_Z \approx \frac{1}{\zeta(3\nu)} \frac{[\eta]\, M_w \eta_s}{N_A k_B T}, \tag{12}$$

where η_s is the viscosity of the solvent, k_B is the Boltzmann constant, and T is the temperature. The pre-factor in Eq. (12) is defined via the Riemann-Zeta function $\zeta(3\nu)$

$= \sum_{i=1}^{\infty} \frac{1}{i^{3\nu}} \approx 0.531$. Taking $\eta_s = 0.162$ Pa s (see Sec. III D), one obtains $\lambda_Z \approx 3.64$ s.

D. Rheological characterisation of the polymer solution

A systematic description of various flow regimes requires an accurate measurement of the control parameter, the Weissenberg number. The measurements of the flow fields via the DPIV tool detailed in Sec. III B allow one to accurately define a scale for the velocity gradients. Equally important for the calculation of *Wi* is the measurement of the relaxation time. For the curvilinear micro-flow, under investigation is a non trivial mixture of shear and extension and it is *a priori* not obvious which method of assessing the largest relaxation time is most relevant. Thus, the best thing one can do at this point is to explore several distinct ways of measuring the relaxation time and estimate the magnitude of the differences one could expect in the resulting Weissenberg number. We focus in this section on a systematic assessment of the relaxation time via four distinct methods.

First, we have characterised the shear rheological behaviour of the polymer solution using a commercial rotational rheometer (Mars III from Thermo Fischer Scientific) equipped with a nano-torque module. The measurements have been performed using a cone plate geometry ($R = 3$ cm, 2° truncation). To prevent the evaporation during long experimental runs, the fluid meniscus has been covered with a thin layer of oil. All rheological measurements have been performed at room temperature ($T_0 = 20$ °C). The shear rate dependence of the shear viscosity is presented in Fig. 2(a) (the squares). The error bars have been calculated by repeating the measurements four times. The viscosity of the solvent was $\eta_s = 0.162\ (\pm 2.6 \cdot 10^{-4})$ Pa s, the circles in Fig. 2(a). The shear thinning behaviour can be described by the Carreau model that provides a first method of formally (the Carreau model is a purely viscous model and does not directly account for elastic effects) estimating a characteristic time scale of the polymer solution:

$$\eta(\dot{\gamma}) = \eta_\infty + (\eta_0 - \eta_\infty)\left[1 + (\lambda_C \dot{\gamma})^2\right]^{(n-1)/2} \tag{13}$$

with $\lambda_c = 1.41\ (\pm 0.028)$ s, $n = 0.623\ (\pm 0.008)$, $\eta_0 = 0.24\ (\pm 0.015)$ Pa s, and $\eta_\infty = 0.17\ \left(\pm 5.1 \cdot 10^{-4}\right)$ Pa s.

A second method of measuring the relaxation time is via measurements of the first normal stress difference $N_1 = \frac{2F_n}{\pi R^2}$. Here F_n is the normal force that has been measured during a separate controlled stress ramp and according to different experimental protocols. As compared with the measurements of the shear viscosity, the measurements of the normal force required some extra points to be considered. First, the reliability of the results is strongly conditioned by the range of shear rates that are explored. Due to the limited accuracy of the force transducer of the rheometer, the lowest shear rate that could be explored was $\dot{\gamma}_{min} \approx 60\ \text{s}^{-1}$. To avoid the emergence of elastic instabilities, the largest shear rate explored was $\dot{\gamma}_{max} \approx 160\ \text{s}^{-1}$. Due to the large values of the shear rate, the raw measurements of the normal force had to be corrected for the inertial contributions (the so-called "*negative normal stress effect*," see Ref. 3) by adding the term $\Delta F_n = \frac{3\pi\rho\Omega^2 R^4}{40}$, where Ω stands for the angular speed of the shaft of the rheometer. Also, to minimize the drift effect of the normal force transducer, prior to modifying the stress, the shaft of the rheometer has been stopped for 300 s allowing the sample to relax and the normal force has been set to 0. Corresponding to each value of the imposed stress, the rate of shear and the normal force were recorded for 300 s, which allowed one to estimate the magnitude of the error bars. The results of the measurements of the first normal stress difference N_1 are presented in the inset of Fig. 2(b). The data scale as a power law $N_1 \propto \dot{\gamma}^{0.92\pm0.11}$ (the full line) rather than quadratically as predicted by the Oldroyd-B model (the dashed line) due to the shear thinning effect clearly visible in Fig. 2(a). Within the framework of the White-Metzner constitutive model[45] and based on the measurements of the first normal stress difference and of the shear viscosity, the relaxation time can be calculated as:

$$\lambda_{NF}(\dot{\gamma}) = \frac{\eta(\dot{\gamma}) N_1(\dot{\gamma})}{2\sigma\dot{\gamma}\left[\eta(\dot{\gamma}) - \eta_s\right]}. \tag{14}$$

The shear rate dependence of the relaxation time calculated according to Eq. (14) is presented in Fig. 2(b). The shear thinning behaviour of the relaxation time can be described by a Carreau type correlation [the line in Fig. 2(b)]:

$$\lambda_{NF} = \lambda_0\left[1 + (\lambda_C \dot{\gamma})^2\right]^{(n-1)/2} \tag{15}$$

with the largest relaxation time $\lambda_0 = 5.5(\pm 1)$s.

A third method of measuring the relaxation time is via capillary breakup extensional rheometry (CaBER).[5] Measurements of the time decay of reduced diameter of the filament of the polymer solution performed with a home-made CaBER

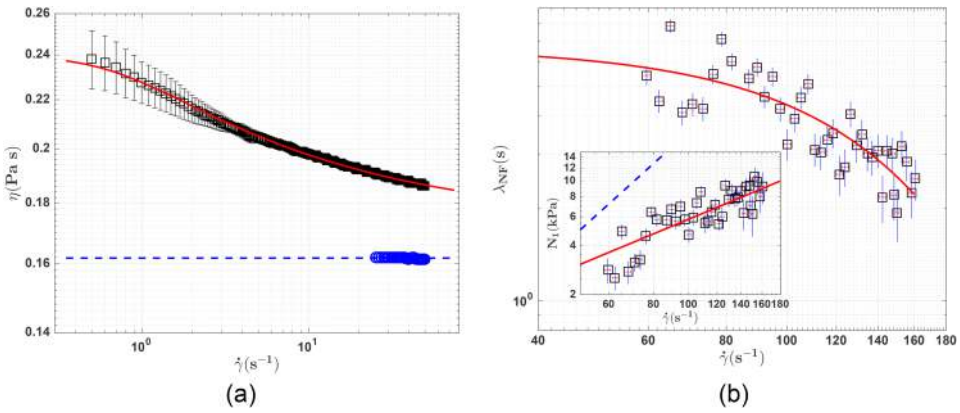

FIG. 2. (a) Dependence of the viscosity of the polymer solution (squares) and solvent alone (circles) measured at room temperature on the shear rate $\dot{\gamma}$. The full line is a fit by the Carreau model. (b) Shear rate dependence of the relaxation time obtained from the measurements of the first normal stress difference, λ_{NF}. The full line is a non-linear fit according to Eq. (15). The shear rate dependence of the first normal stress difference N_1 is presented in the inset. The full line is a power law fit $\lambda_{NF} \propto \dot{\gamma}^{0.92\pm0.11}$ and the dashed line is a guide to the eye, $\lambda_{NF} \propto \dot{\gamma}^2$.

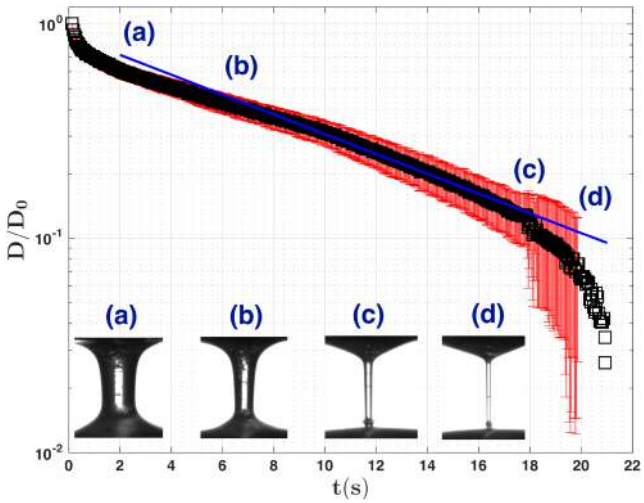

FIG. 3. Time dependence of the normalised diameter of the filament. The full line is an exponential fit, $D/D_0 = 0.88(\pm 0.005) \cdot e^{-t/9.4(\pm 0.047)}$. Sample images of the filament at different stages of the extension are illustrated in the insets.

device are presented in Fig. 3. Images of the filament at various stages of the extensional process are presented in the insets. The error bars have been defined by repeating the measurement four times with a fresh sample. The characteristic decay time t_d measured within the elastic range obtained from an exponential fit (see the line in Fig. 3) may be related to Hookean dumbbell relaxation time via $t_d = 3\lambda_e$[17], which gives in our case $\lambda_e = 3.13(\pm 0.02)$ s.

A fourth method of measuring the relaxation time is by performing small-amplitude oscillatory shear (SAOS) tests. The angular frequency dependence of the relaxation time measured via SAOS is presented in Fig. 4. The relaxation time was calculated from the storage and loss moduli as $\lambda_{SAOS} = \frac{G'}{\omega G''}$. As for the previously discussed rheological measurements, the error bars have been calculated by repeating the experiment several times with fresh samples. One can note that in the limit of small angular frequencies, the largest relaxation time is $\lambda^0_{SAOS} \approx 3$ s.

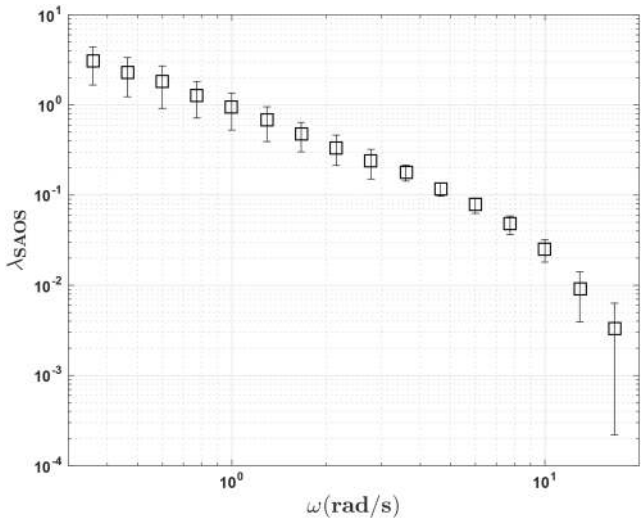

FIG. 4. Frequency dependence of the relaxation time measured via SAOS, λ_{SAOS}.

TABLE I. Summary of the rheological measurements.

Method	Relaxation time (s)	Error (s)
Shear measurements, Carreau fit	1.41	0.028
Normal force measurement, White-Metzner correlation	5.5	1
CaBER	3.13	0.02
SAOS, frequency ramp	3	0.3
SAOS, single mode Maxwell fit, data from Ref. 7	5	0.5
Torque relaxation, data from Ref. 42	4.5	0.2

The results of the rheological measurements presented through this section and some previous measurements from the literature are summarised in Table I. One can note that, regardless of the measuring method, the relaxation time is of order of unity. We propose to use for the calculation of the Weissenberg number through the rest of the paper an average of the results summarised in Table I, $\bar{\lambda} = 3.75$ s. The standard deviation of these distinct measurements is $\lambda_{rms} = 1.52$ s. We note that this average value is very close to the estimate of the Zimm relaxation time given in Sec. III C, $\lambda_Z \approx 3.64$ s. The global Weissenberg number is calculated as $Wi = 2\bar{\lambda}U_\theta^{max}/W$, where U_θ^{max} is the maximum value of the tangential component of the flow velocity. The Reynolds number is calculated as $Re = \rho U_\theta^{max} W/\eta$ and, for the experiments reported herein, never exceeded $4 \cdot 10^{-4}$, which indicates that inertial effects were practically absent.

E. Assessment of the reliability of the measurement technique

As we aim to provide a systematic characterisation of the transition to elastic turbulence in a curvilinear micro-channel flow as well as a full description of the spatio-temporal features of the flow in a regime of fully developed elastic turbulence, it is crucial to test the reliability of the DPIV technique. For this purpose, we have conducted two distinct calibration experiments.

First, we have measured long time series (during 600 s) of flow fields of the polymer solution in a straight micro-channel with a width $W = 200$ μm, depth $H = 200$ μm, and total length $L = 5$ cm.

An analytical solution for the transient pressure driven plane-channel flow of an Oldroyd-B fluid was first obtained for low Re by Waters and King in the early 1970s.[44] An important conclusion of their study is that in the asymptotic time limit, the steady state part of the solution practically coincides with the analytical solution for a Newtonian fluid:

$$U(x) = \frac{W^2}{8\eta}\frac{\Delta p}{L}\left[1 - \left(\frac{2x}{W}\right)^2\right]. \quad (16)$$

Here x is the coordinate transversal to the flow direction and Δp stands for the driving pressure drop. For an Oldroyd-B fluid flowing at low Re in a channel with a rectangular cross section, a full analytical solution for the time dependent axial velocity has been derived in Ref. 18. As this solution is mathematically more involved and we measure the flow fields at the mid-plane of the micro-channel where the corner effects are

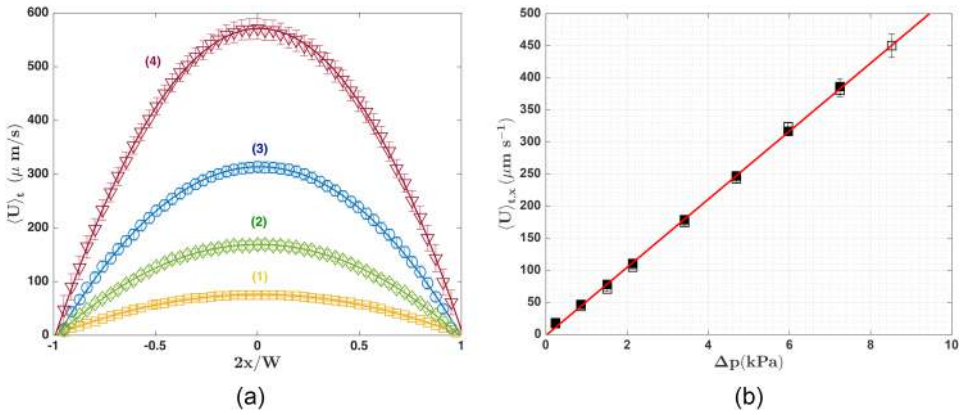

FIG. 5. (a) Time averaged transversal profiles of the axial velocity measured in a straight micro-channel with the polymer solution for several driving pressures Δp: (1–yellow squares) $\Delta p = 1.9$ kPa, (2–green diamonds) $\Delta p = 2.55$ kPa, (3–blue circles) $\Delta p = 3.8$ kPa, (4–dark red down triangles) $\Delta p = 7.65$ kPa. For clarity of the presentation, the spatial resolution of each data set has been decreased by a factor of 2. The full lines are parabolic fit functions (see text for description). (b) Dependence of the time averaged mean flow speed measured with the polymer solution in a straight micro-channel on the driving pressure Δp. The full/empty symbols refer to increasing/decreasing pressures and the full line is a linear fit.

less pronounced, we retain for validation purposes the simpler plane-channel solution given by Eq. (16).

Measurements of the time averaged transversal profiles of the axial velocity $\langle U \rangle_t$ performed for several driving pressures are presented in Fig. 5(a). The error bars are defined by the root mean square deviation of the velocity time series and never exceeded 5% of the mean flow velocity. The velocity profiles are symmetric with respect to the centre line of the channel $x = 0$ and, within the instrumental accuracy of the DPIV measurements, no apparent slip was observed in the vicinity of the channel's walls (each transversal velocity profile extrapolates to 0 at the walls $2x/W = \pm 1$). Moreover, each individual velocity profile can be accurately fitted by the analytical solution given by Eq. (16)—the full lines in Fig. 5(a).

The axial flow speed averaged both in time and across the channel width $\langle U \rangle_{t,x}$ depends linearly on the driving pressure drop Δp, Fig. 5(b), and the measurements performed at increasing/decreasing pressure (the full/empty symbols) fully overlap.

As a second test of the reliability of the measurement technique, we have investigated the flow of the solvent alone in the curvilinear micro-channel by acquiring time series of flow fields for various driving pressures, Fig. 6. The total data acquisition time was the same as that for the experiments performed in the straight channel described above. Several time averaged transversal profiles of the tangential velocity component $\langle U_\theta \rangle_t$ are exemplified in Fig. 6(a). The reduced radial coordinate is defined as $\xi = 1 + \frac{2(r-R_2)}{W}$, where r is the radial coordinate [see the top inset in Fig. 1(a)]. As compared with the measurements performed with the polymer solution in a straight channel, the flow profiles are no longer symmetric with respect to the centre line of the channel $\xi = 0$, which is due to the curvilinear geometry of the channel. As in the previous test case, the velocity fluctuations were solely related to the instrumental error of the DPIV measurements and never exceeded 5% of the mean flow speed. The time averaged mean flow speed depends linearly on the driving pressure drop and, consistently with a linear and laminar flow, this dependency is reversible upon increasing/decreasing pressures—the full/empty symbols in Fig. 6(b).

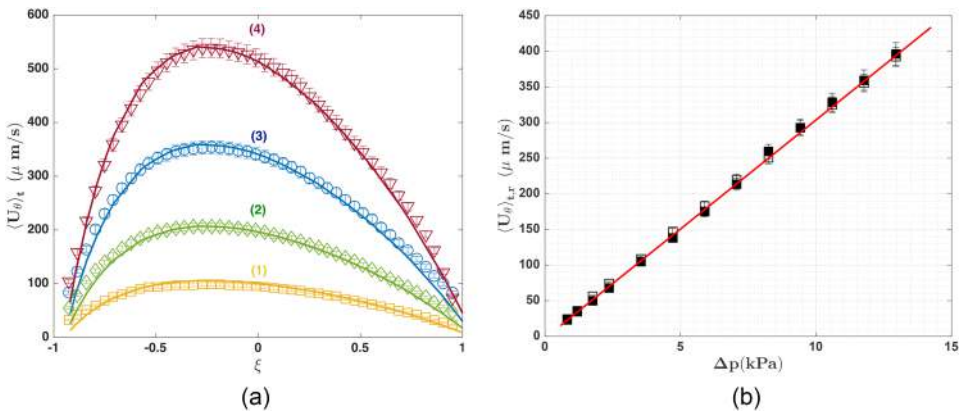

FIG. 6. (a) Time averaged transversal profiles of the tangential velocity component measured with the solvent alone in the curvilinear micro-channel for several driving pressures Δp: (1–yellow squares) $\Delta p = 2.35$ kPa, (2–green diamonds) $\Delta p = 4.7$ kPa, (3–blue circles) $\Delta p = 8.24$ kPa, (4–dark red down triangles) $\Delta p = 13$ kPa. For clarity of the presentation, the spatial resolution of each data set has been decreased by a factor of 2. The full lines are the results of 3D numerical simulations performed with Comsol Multiphysics. (b) Dependence of the time averaged mean flow speed measured with the solvent alone in the curvilinear micro-channel on the driving pressure Δp. The full/empty symbols refer to increasing/decreasing pressures and the full line is a linear fit.

These results are in good qualitative agreement with the measurements performed with a Newtonian fluid in a millimetre size serpentine by Jun and Steinberg[25] (Figs. 2 and 3 therein) and with the numerical simulations performed by Abed and co-workers.[1]

For a quantitative validation, we have performed 3*D* numerical simulations using Comsol Multiphysics—the full lines in Fig. 6(a). A fair agreement is found between the measurements and the simulation results.

The overall conclusion of the data presented in Figs. 5 and 6 is that in a range of flow speeds relevant to the experiments performed with the polymer solution in the curvilinear micro-channel, both the plane channel flow of the polymer solution and the flow of the solvent alone in the curvilinear micro-channel are found to be linear, laminar, fully reversible upon increasing/decreasing driving pressures, and steady. The observed velocity fluctuations are solely related to the instrumental error of the *DPIV* technique, and their magnitude is significantly lower than the magnitude of fluctuations typically observed in an elastic turbulent flow.

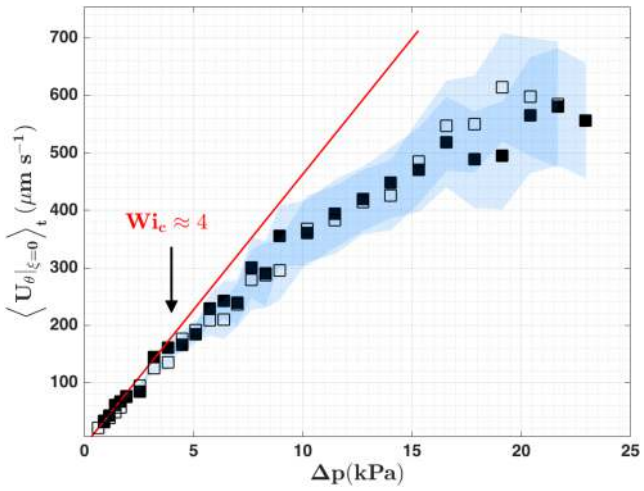

FIG. 8. Dependence of the time averaged tangential velocity component on the driving pressure (bottom horizontal axis) and on the global Weissenberg number (top horizontal axis). The full/empty symbols refer to the increasing/decreasing branches of the pressure ramp. The shaded regions highlight the level of fluctuations. The full line is a linear fit.

IV. RESULTS

A. Onset and development of the elastic turbulence, flow structure

A visual assessment of the hydrodynamic stability of the flow is illustrated in Fig. 7 by means of the streak imaging technique. Whereas a laminar flow is observed for low values of the driving pressure $\Delta p = 63$ Pa [panel (a)], a strongly irregular fluid motion is observed corresponding to $\Delta p = 2.3$ kPa [panel (b)]. At this driving pressure, a major re-organisation of the flow is apparent in the form of a large scale non-stationary spiral vortex in agreement with the observation performed by means of laser scanning confocal microscopy reported in Ref. 7.

Measurements of the dependence of the time averaged tangential velocity component measured at the centre line of the channel ($\xi = 0$) on the driving pressure (global Weissenberg numbers) are presented in Fig. 8. The average was carried on over 1200 s (a time roughly 320 times longer than the average relaxation time of the polymer $\bar{\lambda}$), which guarantees that the flow field information is statistically sufficient.

The dependence of the time averaged tangential flow component $\langle U_\theta \rangle_t$ on the Weissenberg number remains roughly linear up to a critical value $Wi_c \approx 4$—the full line in Fig. 8. Above this critical value, the data fall below the linear dependence observed in a laminar regime indicating a significant re-organisation of the flow associated with an elastic flow instability. It is noteworthy that the transition to elastic turbulence is smooth and, within the instrumental accuracy of the measurements, reversible upon increasing/decreasing pressure drops (the full/empty symbols in Fig. 8) (note the overlap of the full/empty symbols). The value of the critical Weissenberg number is comparable to the values reported in Refs. 7–9. However, a significantly larger discrepancy is found with the onset value given in the recent paper by Jun and Steinberg,[25] $Wi_c \approx 200$. This difference cannot be explained by the different aspect ratio of the channel ($R_1/W = 1$) using the Pakdel-McKinley scaling.[31,46] As they have used a similar polymer solution, the reasons for this discrepancy remain elusive.

To get further insights into the evolution of the flow structure as the global Weissenberg number is increased, we focus on the time averaged transversal profiles of each velocity component, Fig. 9.

At low driving pressures corresponding to the laminar flow regime, the profile of the tangential velocity component $\langle U_\theta \rangle_t$ is non-symmetric [the circles in Fig. 9(a)] and qualitatively similar to the velocity profiles measured with the solvent alone, Fig. 6(a). Due to the curvilinear geometry of the micro-channel, a non-zero time averaged radial component $\langle U_r \rangle_t$ is measured even in a laminar state, Fig. 9(b). An increase of the Weissenberg number past the onset of the primary elastic instability results in a significant re-organisation of the flow:

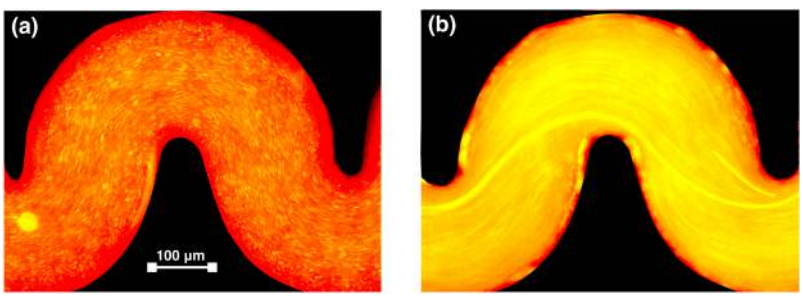

FIG. 7. Epifluorescent flow micrographs acquired at (a) $\Delta p = 63$ Pa ($Wi = 0.36$—laminar regime) (b) $\Delta p = 2.3$ kPa ($Wi = 18$—elastic turbulent regime). A $X10$ magnification objective was used.

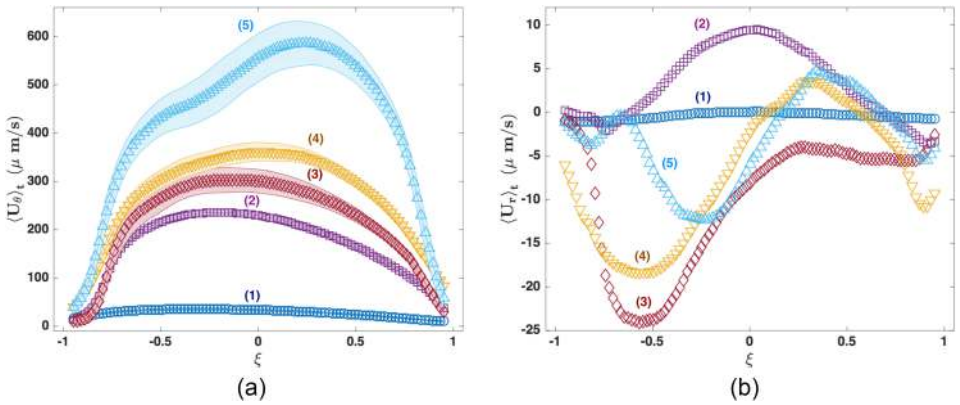

FIG. 9. Time averaged transversal profiles of the tangential velocity component [panel (a)] and of the radial velocity component [panel (b)]. The symbols in panels refer to the driving pressures (global Weissenberg number): (1–blue circles) Δp = 0.9 kPa (Wi = 1.1), (2–violet squares) Δp = 5.7 kPa (Wi = 7.4), (3–dark red diamonds) Δp = 7.6 kPa (Wi = 9.5), (4–yellow down triangles) Δp = 10.2 kPa (Wi = 11.3), (5–blue triangles) Δp = 23 kPa (Wi = 18.3). The shaded regions in (a) indicate the level of fluctuations of the velocity around its mean.

the transversal profiles of the tangential velocity component become more symmetric and a strong inwards radial motion is observed. The flow structure illustrated in Fig. 9 is qualitatively consistent with that observed by the particle tracking velocimetry measurements presented in Ref. 7.

The time series of both the tangential and the radial components of the flow velocity measured at the centre line of the curvilinear micro-channel ($\xi = 0$) are presented in Fig. 10. In a laminar regime (the time series labelled by a circle and square, respectively), the fluctuations visible in the time series of each velocity component are solely related to the instrumental error of the micro-PIV technique fully documented in Sec. III E. As the Weissenberg number is increased, the velocity time series exhibit a chaotic like behaviour that reproduces the early measurements reported in Refs. 7 and 8. As the measurements illustrated in Figs. 10(a) and 10(b) are performed over a total time 12 times larger than the acquisition time in Refs. 7 and 8, we are now able to observe a new dynamical flow feature in the form of rare "flight-crash" events manifested by a significant slowing down of the flow [see the series labelled by a rhomb and a down triangle in Fig. 10(a)]. These rare events emerge right above the onset of the primary elastic instability and the frequency of their appearance increases with increasing control parameter. A closer look into the emergence of rare events near the onset of the elastic turbulence is presented in Fig. 11 by monitoring instantaneous flow fields (the bottom line) before, during, and after the emergence of a rare event.

One can note that a rare event is associated with a dramatic re-organisation of the flow that persists for times significantly larger than the average polymer relaxation time, $\Delta T \approx 250$ s. The emergence of rare events has been previously observed during experiments performed on a macroscopic von Karman swirling flow between two disks of a dilute polymer solution.[11] In contrast to the observation illustrated in Fig. 11, in a von Karman flow, the rare events are manifested though a local flow acceleration rather than a deceleration, see Figs. 20(a) and 21(a) in Ref. 11. The difference may originate in the different type of forcing of the two flows. Whereas the measurements of the velocity time series in the von Karman swirling flow were performed at a controlled angular speed Ω of the top disk (which sets the scale for the rate of deformation $\dot{\gamma}$), the microscopic flows presented here are driven at constant pressures, i.e., at constant applied stresses. This explanation is corroborated by the different orientation of the skewness of the probability distributions of the injected power corresponding to the two distinct forcing modes, see Figs. 5–7 in Ref. 11. In both cases, however, the frequency of the emergence of rare events increases with increasing global Weissenberg numbers indicating a similar physical origin.

The spatial distributions of the reduced fluctuations of the velocity modulus $\frac{U_{rms}}{\langle U \rangle_t}$ measured for four distinct values of the Weissenberg number are illustrated in Fig. 12. Above the onset of elastic turbulence, a spatially inhomogeneous but smooth field of velocity fluctuations is observed. This distribution indicates a strong spatial correlation of the random flow, and its topology reflects the main spiral vortical flow structure of the random flow.

The dependence of the rms of fluctuations of each velocity component measured at the centre line of the micro-channel

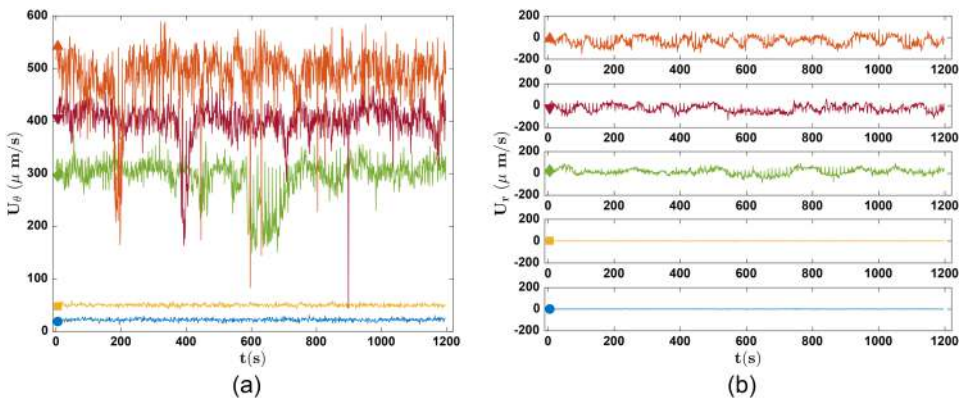

FIG. 10. Time series of the tangential [panel (a)] and the radial velocity components [panel (b)] measured at the mid-point of the channel ($\xi = 0$) at half depth. The symbols in panels refer to the driving pressure (Weissenberg number): Blue circle–Δp = 0.9 kPa (Wi = 1.1), yellow square–Δp = 5.7 kPa (Wi = 7.36), green diamond–Δp = 7.6 kPa (Wi = 9.5), dark red down triangle–Δp = 10.2 kPa (Wi = 11.3), orange up triangle–Δp = 23 kPa (Wi = 18.3).

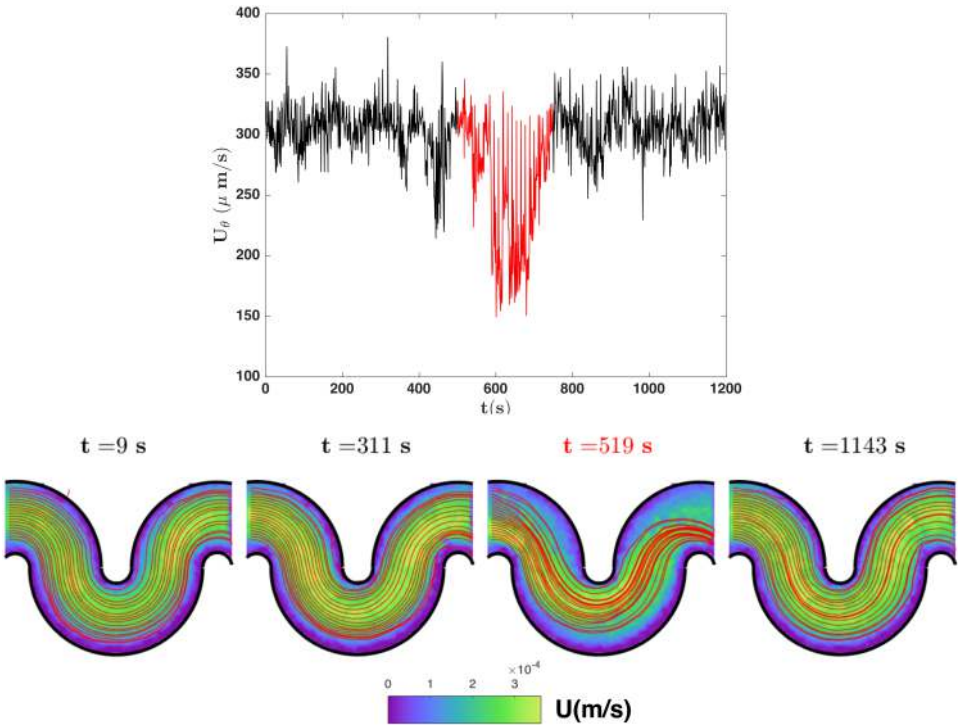

FIG. 11. Top: Time series of the tangential velocity component acquired at $Wi = 9.5$ at the centre-line $\xi = 0$ of the curvilinear micro-channel. Bottom: Maps of the velocity modulus at several time instants indicated on the top. The full lines in each bottom panel are streamlines.

on the Weissenberg number is presented in Fig. 13. A strong increase of the level of fluctuations of both the tangential velocity component Fig. 13(a) and the radial velocity component Fig. 13(b) accounting for up to 35% of the mean flow speed is observed.

As already noted for the Weissenberg dependence of the time averaged tangential velocity component presented in Fig. 8, the transition is smooth and, within the level of scatter of the data, reversible upon increasing/decreasing Wi. Moreover, the data can be fitted by the stationary Landau-Ginzburg equation with a field [the full lines in Figs. 13(a) and 13(b)]:

$$\epsilon U_i^{rms} - a\left(U_i^{rms}\right)^3 + h = 0 \quad i = r, \theta, \tag{17}$$

where $\epsilon = Wi/Wi_c - 1$ is the reduced control parameter, and a and h are fitting parameters. One can conclude that the transition to elastic turbulence in a curvilinear micro-flow occurs via a supercritical bifurcation. This result is interesting in itself, somewhat unexpected, and it deserves being discussed. In a Taylor-Couette geometry, the elastic instability is experimentally found to emerge via a subcritical bifurcation[20] in agreement with the theoretical prediction.[40] A systematic and pedagogical description of the subcritical elastic instability in parallel shear flows of viscoelastic fluids is presented in Ref. 32. The early investigation of the transition to elastic turbulence in a von Karman swirling flow between disks suggested a similar subcritical bifurcation in the form of a

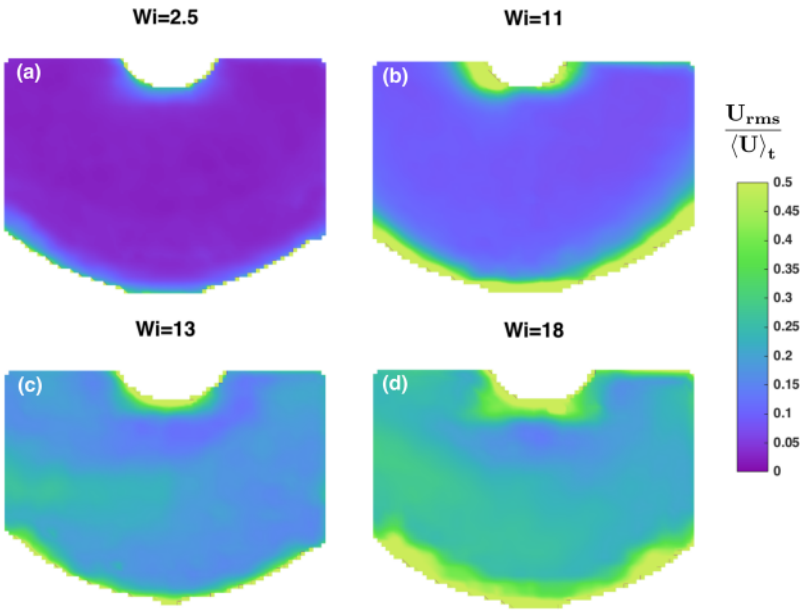

FIG. 12. Spatial distribution of the reduced velocity fluctuations $\frac{U_{rms}}{\langle U \rangle_t}$ measured at different Weissenberg numbers indicated in the top insets.

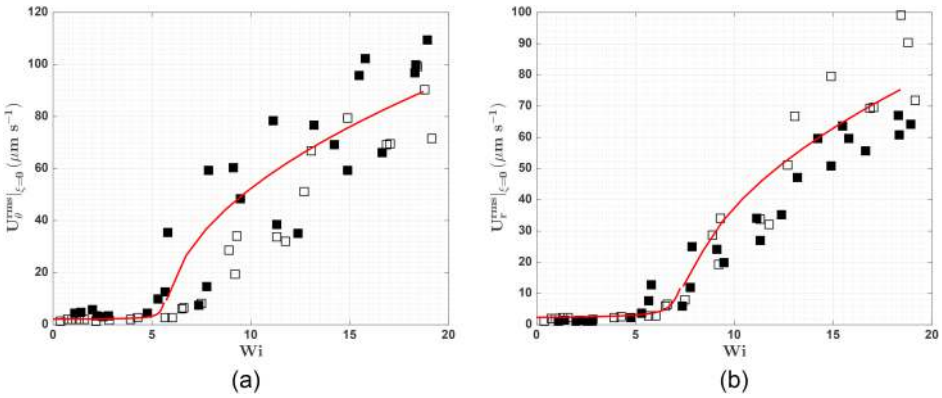

FIG. 13. Dependence of the rms of fluctuations of the tangential velocity component [panel (a)] and of the radial velocity component [panel (b)] measured at the midpoint of the channel ($\xi = 0$) on the global Weissenberg number *Wi*. The full/empty symbols refer to the increasing/decreasing driving pressures. The full line in each panel is a fit by the stationary Ginzburg-Landau equation (see text for description).

hysteresis of the time averaged injected power (calculated as the product between the angular speed of the top disk and the torque that drives it).[7,13,14] However, more recent measurements of the power injected into a von Karman swirling flow averaged over significantly longer times reported in Ref. 42 revealed a smooth and reversible transition consistent with a supercritical bifurcation, see Fig. 4 therein. To conclude this part, the nature of the transition to elastic turbulence remains elusive, and future theoretical and numerical studies are needed to clarify this point.

B. Statistics and spatial distribution of the velocity gradients; analysis of boundary layers

As pointed out in Sec. II, the key physical quantities that need to be measured in order to verify the predictions of the theory of elastic turbulence are the time averaged fields of the velocity gradients and their level of fluctuation. Particularly, the production of the elastic stresses that destabilise the flow is directly related to the magnitude of the velocity gradients and the level of their fluctuations, and one of the key ingredients of the theory of elastic turbulence relates to the saturation of the rms of fluctuations of the velocity gradients due to a strong back reaction of the polymers to the flow. This motivates us to take advantage of the excellent temporal and spatial resolution of the DPIV method described in Sec. III to provide a full description of the spatial distribution of the velocity gradients and the long time statistics of their fluctuations.

The spatial distributions of the time averaged second invariant of the rate of strain $\left\langle \dot{\underline{\underline{\gamma}}} \right\rangle_t$ measured for three distinct Weissenberg numbers are presented in Fig. 14. One can note that the spatial distribution of the second invariant of the rate of strain is strongly inhomogenous and exhibits pronounced local maxima of unequal magnitude [except for the highest *Wi* illustrated in panel (d)] distributed at a constant distance from the inner and outer boundaries of the channel, panel (a) in Fig. 14. As the extension of the linear polymer chains is controlled by the local velocity gradients, we attribute the observation of the local maxima of the velocity gradients to the formation of inner and outer boundary layers of the elastic stresses.

The primary elastic instability is accompanied by a sharp increase of the velocity gradients particularly in the vicinity of the inner boundary of the channel, panel (b) in Fig. 14. The lack of symmetry of the spatial distribution of the velocity gradients with respect to the centre line of the micro-channel indicates a

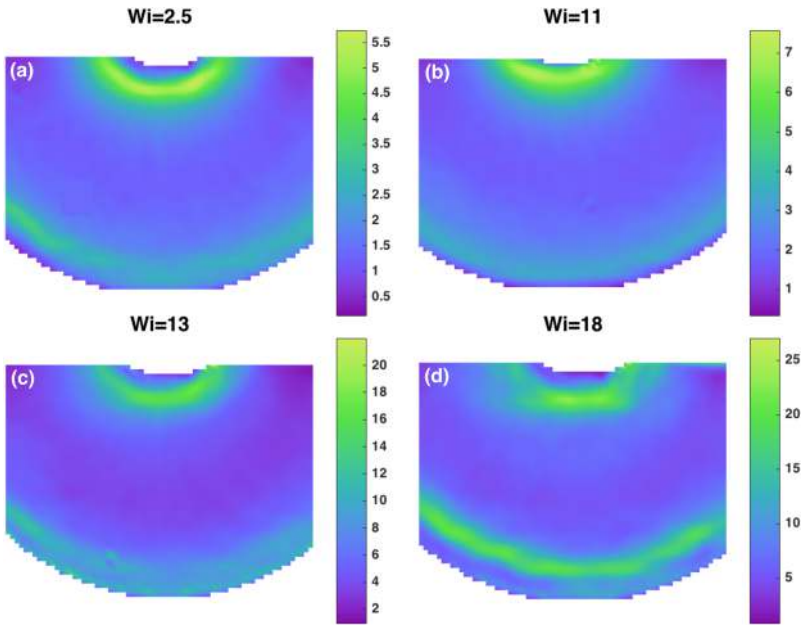

FIG. 14. Spatial distribution of the time averaged second invariant of the rate of strain $\left\langle \dot{\underline{\underline{\gamma}}} \right\rangle_t$ measured at different Weissenberg numbers indicated in the top insets. The units of the color-bars are s^{-1}.

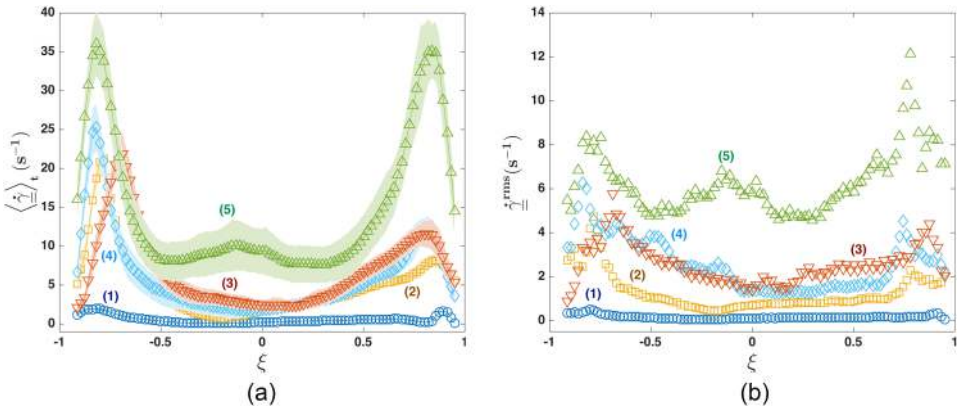

FIG. 15. Transversal profile of the time averaged second invariant of the rate of deformation (a) and of the rms of fluctuations of the second-invariant (b) measured at various driving pressures (global Weissenberg numbers): (1–navy blue circles) $\Delta p = 0.9$ kPa ($Wi = 1.1$), (2–yellow squares) $\Delta p = 5.7$ kPa ($Wi = 7.3$), (3–blue diamonds) $\Delta p = 7.6$ kPa ($Wi = 9.5$), (4–red down triangles) $\Delta p = 10.2$ kPa ($Wi = 11.3$), (5–green triangles) $\Delta p = 23$ kPa ($Wi = 18.3$). The shaded regions in (a) indicate the level of fluctuations around the mean value.

strongly inhomogeneous distribution of elastic stresses along the transversal flow direction. Within a fully developed elastic turbulent regime, the symmetry of the distribution of the elastic stresses with respect to the centre line of the channel is restored. A more systematic investigation of the transversal distribution of the time averaged velocity gradients and of their fluctuations as a function of the global Weissenberg number is presented in Fig. 15.

The emergence of a boundary layer of the elastic stresses when the global Weissenberg number is increased is clearly visible in Fig. 15(a). As already noted in Fig. 14, as one advances within the regime of fully developed elastic turbulence, the two local maxima of the profiles of the time averaged gradients tend to become equal in magnitude. Corresponding to the edge of the boundary layers, local maxima are also observed in the transversal distributions of the rms of fluctuations of the second invariant of the rate of deformation tensor, Fig. 15(b).

The evolution of the width of the inner and outer boundary layers determined by the location of the peaks of the spatial distribution of the time averaged second invariant of the rate of strain tensor [Fig. 15(a)] with the global Weissenberg number is presented in Fig. 16. The width of the inner boundary layer (the squares) is systematically larger than the width of the outer boundary layer (the circles) up to a Weissenberg number $Wi \approx 15$ corresponding to the fully developed elastic turbulent regime when the two boundary layers become practically identical.

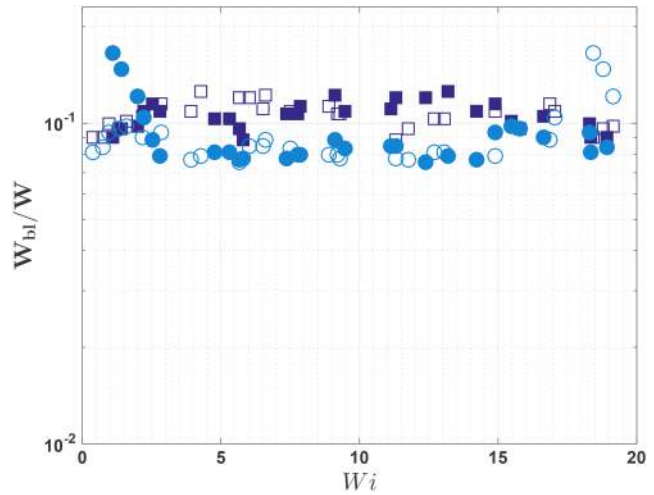

FIG. 16. Dependence of the reduced width of the inner boundary layer (empty navy blue squares and filled navy blue squares) and of the outer boundary layer (filled blue circles, empty blue circles) on the global Weissenberg number. The full/empty symbols refer to increasing/decreasing global Weissenberg numbers, respectively.

We note that within a regime of elastic turbulence, the width of the inner and outer boundary layers is $W_{bl}/W \approx 0.1$ and independent of the global Weissenberg number. This result is consistent with the measurements presented by Jun and Steinberg[25] and with earlier measurements performed in a macroscopic von Karman swirling flow.[7,14]

The evolution of the time averaged velocity gradients and of the local Weissenberg number defined as $Wi_{loc} = \bar{\lambda}\dot{\bar{\gamma}}^{rms}$ measured at the edge of the inner/outer boundary layers [corresponding to the local maxima in Figs. 15(a) and 15(b)] and in the bulk of the flow (averaged around the centre line of the micro-channel) with the global Weissenberg number is presented in Fig. 17.

The primary elastic instability is accompanied by a sharp increase of both the time averaged velocity gradients [panel (a)] and of the local Weissenberg number [panel (b)]. For $Wi \leq 17$, the time averaged velocity gradients measured at the edge of the inner boundary layer are systematically larger than those measured at the edge of the outer boundary layer, Fig. 17(a). The local Weissenberg number measured at the edge of the inner boundary layer is systematically larger than the one measured at the centre line of the flow, Fig. 17(b). Within a fully developed elastic turbulent regime, the local Weissenberg number measured at the edge of the boundary layers increases linearly with the global Weissenberg number $Wi_{loc}^{bl} = -25.58 + 3.54Wi$ [the dashed line in Fig. 17(b)]. On the other hand, a linear fit of the local Weissenberg number measured in the bulk of the flow gives $Wi_{loc}^{bulk} = 15.21 + 0.12Wi$ [the full line in Fig. 17(b)]. Thus, one can conclude that in a fully developed elastic turbulence regime, Wi_{loc} saturates in the bulk of the flow but keeps increasing at the edge of the boundary layers. The result is in qualitative agreement with the theoretical prediction for elastic turbulence.[2,19] Corresponding to the bulk measurements, one obtains $Wi_{loc}^{bulk} \approx 15.5$, which is significantly larger than the unitary value $Wi_{loc} \approx 1$ predicted theoretically indicating that no quantitative agreement with the theory is found.

This is an interesting experimental fact that deserves a separate discussion. To get further insights, we compare in the

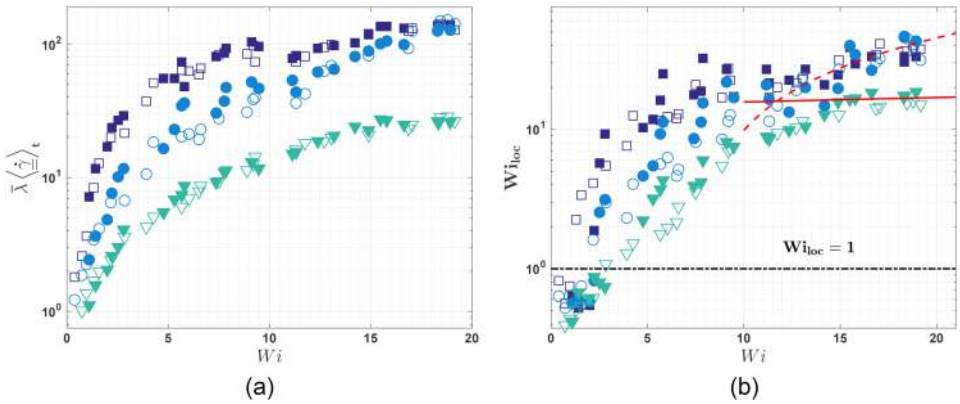

FIG. 17. (a) Dependence of the time averaged second invariant of rate of deformation on the global Weissenberg number. (b) Dependence of the local Weissenberg number Wi_{loc} on the global Weissenberg number. The full and dashed lines are linear fit functions (see text for description). In both panels, the symbols refer to different radial locations ξ of the measurements: (empty navy blue squares and filled navy blue squares) the edge of the inner boundary layer, (filled blue circles and empty blue circles) the edge of the outer boundary layer, (filled green down triangles and empty green down triangles) average in the bulk of the flow within the range $\xi \in [-0.4, 0.4]$. In both panels, the full/empty symbols refer to increasing/decreasing global Weissenberg numbers, respectively.

following the result on the saturation of Wi_{loc} with previous experimental results.

A similar conclusion on the saturation of the rms of the fluctuations of the velocity gradients has been reached for the case of an elastic turbulent flow in a macroscopic von Karman swirling flow configuration (the diameter of the vessel was $D = 9.8$ cm).[7,11,13] The local Weissenberg number was defined in these references as $Wi_{loc} = \omega^{rms}\lambda$ (here ω stands for vorticity) saturates at the value $Wi_{loc} \approx 2$ [Fig. 19(b) in Ref. 11, inset of Fig. 2 in Ref. 13], which is twice larger than the value predicted by the theory. For the case of a macroscopic von Karman swirling flow studied in Refs. 7, 11, and 13, the width of the boundary layer was measured to be $W_{bl} \approx 0.46$ mm, which accounts for 0.47% of the dominant space scale L of the system (see Fig. 30 therein). As compared to this, the width of the boundary layer measured in the curvilinear micro-flow studied herein accounts for 10% of the dominant space scale W of the micro-flow (see Fig. 16). The measurements performed in a microscopic von Karman swirling flow by Liu and Steinberg revealed a saturation of both the local Weissenberg number and the polymer contribution to the stress tensor at a value significantly larger than unity[29] $Wi_{loc} \in [10, 100]$ (see Fig. 4 and the inset in Fig. 5 therein). These experimental facts suggest that the quantitative discrepancy with the theory of elastic turbulence might be related to spatial confinement of the flow: in microscopic flow systems, the presence of the boundary layers where the rms of the gradients increase monotonically with Wi influences the dynamics in the bulk of the flow shifting the saturation value of Wi_{loc} at values significantly larger than one. This effect is much less pronounced in a macroscopic flow system with a size much larger than the width of the boundary layer. Whereas the conclusion on the saturation of the rms of the fluctuations of the velocity gradients measured in the bulk of the flow is consistent with a number of earlier experimental findings, a clear disagreement is found with the recent measurements performed by Jun and Steinberg in a millimetre size serpentine channel.[25] In this paper, a nearly linear increase of Wi_{loc} with Wi is found, Figs. 7, 8, and 20 therein. Although we do not have a clear understanding of the reasons for this discrepancy, we can note that as their onset of elastic instability was surprisingly large $Wi_c \approx 200$, their measurements were performed at much larger Wi, $Wi \in [200, 950]$.

Finally, we note that the measurements of the time averaged velocity gradients and of the rms of their fluctuations are reproducible upon increasing/decreasing Wi, proving once more the reversibility of the bifurcation towards elastic turbulence (the full/empty symbols in Fig. 17) in a curvilinear microchannel flow in full agreement with the behaviour observed in Figs. 8 and 13.

C. Spatial and temporal correlations of the fluctuations of the microscopic flow fields

The high temporal and spatial resolution of the *DPIV* measurements allows one to quantitatively assess the temporal and spatial correlations of the fluctuations of the flow over the entire range of global Weissenberg number.

The spatial correlation functions of each velocity component are defined according to:

$$C_{U_i}(\delta\xi) = \frac{\left\langle u_i'(\xi+\delta\xi)u_i'(\xi)\right\rangle_\xi}{\left\langle \left(u_i'(\xi+\delta\xi)\right)^2\right\rangle_\xi}, \quad i = \theta, r, \tag{18}$$

where the fluctuating parts of each velocity component are $u_i'(\xi) = U_i(\xi) - \langle U_i(\xi)\rangle_\xi$, and $\delta\xi$ is the distance between two neighbouring points in the flow defined in terms of the reduced radial coordinate ξ.

The spatial correlations of fluctuations of each velocity component along the transversal flow direction ξ are presented in Fig. 18.

The spatial correlations of the fluctuations of the tangential flow component do not depend on the Weissenberg number Fig. 18(a) and decay logarithmically to zero over a distance $\xi \approx 0.2$. The local minima of the spatial correlation functions probably correspond to the edge of the inner/outer boundary layers illustrated in Fig. 17. The spatial correlation of the fluctuations of the transversal velocity component is more sensitive to the global Weissenberg number, Fig. 18(b). Within a regime of fully developed elastic turbulence, the anti-correlated part

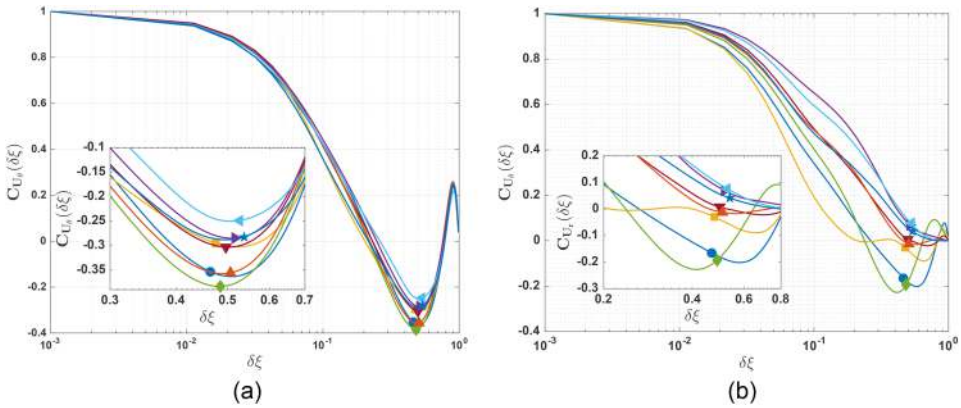

FIG. 18. (a) Spatial correlation functions of the tangential component of the velocity U_θ. (b) Spatial correlation functions of the radial component of the velocity U_r. In both panels, the symbols refer to the driving pressures (Weissenberg numbers): circle-Δp = 1.9 kPa (Wi = 2.5), yellow square–Δp = 4.5 kPa (Wi = 5.66), navy blue diamond–Δp = 5.7 kPa (Wi = 7.4), red down triangle–Δp = 7.66 kPa (Wi = 9.5), orange triangle–Δp = 10.2 kPa (Wi = 11.3), blue left triangle–Δp = 12.77 kPa (Wi = 13.2), violet right triangle–Δp = 19.11 kPa (Wi = 15.66), navy blue star–Δp = 23 kPa (Wi = 18.33). A magnified view of the data is presented in the insets.

of the correlation functions vanishes and the fluctuations of the radial component remain highly correlated over more than half width of the micro-channel. The tangential velocity component is strongly correlated along the transversal flow direction and the correlation functions are practically independent of the Weissenberg number, Fig. 18(a). The measurements of the spatial correlation functions qualitatively agree with the measurements by Jun and Steinberg[25] (Fig. 23 therein), in the sense that the fluctuations of the tangential velocity component are overall more correlated than those of the radial velocity component.

The temporal correlation functions of the fluctuating part of each velocity component are defined according to:

$$C_{U_i}(\tau) = \frac{\left\langle u_i'(t+\tau)u_i'(\tau)\right\rangle_t}{\left\langle \left(u_i'(t)\right)^2\right\rangle_t}, \quad i = \theta, r, \tag{19}$$

where the fluctuating parts of each velocity component are $u_i'(t) = U_i(t) - \langle U_i(t)\rangle_t$.

The temporal autocorrelation functions of the tangential and radial velocity components of the flow field measured at the centre line of the channel are presented in Figs. 19(a) and 19(b).

The measurements of the temporal auto correlation functions allow one to estimate the correlation times of each velocity component as $\tau_c^i = \frac{\int_0^{T_{max}} t|C_i(t)|dt}{\int_0^{T_{max}} |C_i(t)|dt}$, where $i = \theta, r$ and T_{max} = 1200 s is the total data acquisition time of the series of velocity fields.

The dependence of the correlation times of the fluctuations of both the tangential (the squares) and the radial (the circles) velocity components measured in the bulk of the flow on the Weissenberg number is presented in Fig. 20(a). Whereas the fluctuations of the tangential velocity remain strongly correlated regardless of the value of Wi, the fluctuations of the radial component de-correlate quickly as Wi is increased past the onset of elastic turbulence. In a regime of fully developed elastic turbulence, the radial correlation time saturates with Wi at $\tau_r^c \approx 13\bar{\lambda}$. This result disagrees with both previously found for the case of a macroscopic von Karman swirling flow in Refs. 7 and 14 or a millimetre size serpentine channel in Ref. 25 and the theory that predicts $\tau_c \approx \bar{\lambda}$.

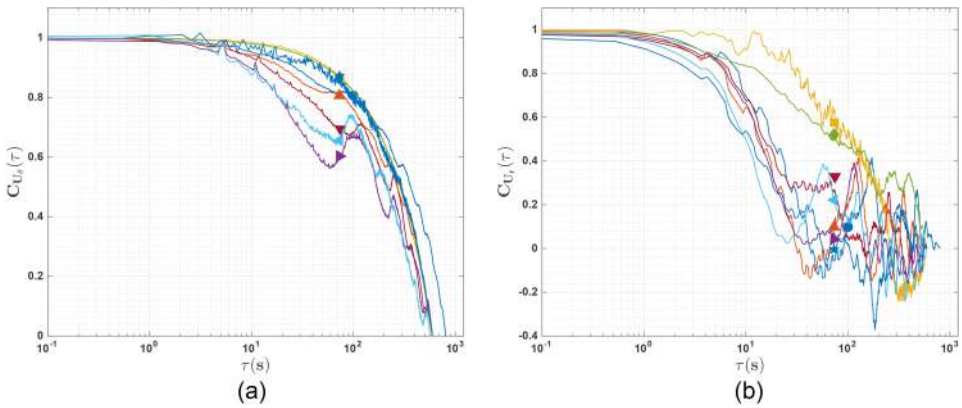

FIG. 19. Time auto-correlation functions of the tangential component of the velocity U_θ [panel (a)] and of the radial component of the velocity U_r measured at centre line of the micro-channel (ξ = 0). (b) In both panels, the symbols refer to the driving pressures (Weissenberg numbers): blue circle–Δp = 1.9 kPa (Wi = 7.6), yellow square–Δp = 4.5 kPa (Wi = 2.5), navy blue diamond–Δp = 5.7 kPa (Wi = 7.4), red down triangle–Δp = 7.66 kPa (Wi = 9.5), orange triangle–Δp = 10.2 kPa (Wi = 11.33), blue left triangle–Δp = 12.77 kPa (Wi = 13.2), violet right triangle–Δp = 19.11 kPa (Wi = 15.66), navy blue star–Δp = 23 kPa (Wi = 18.33).

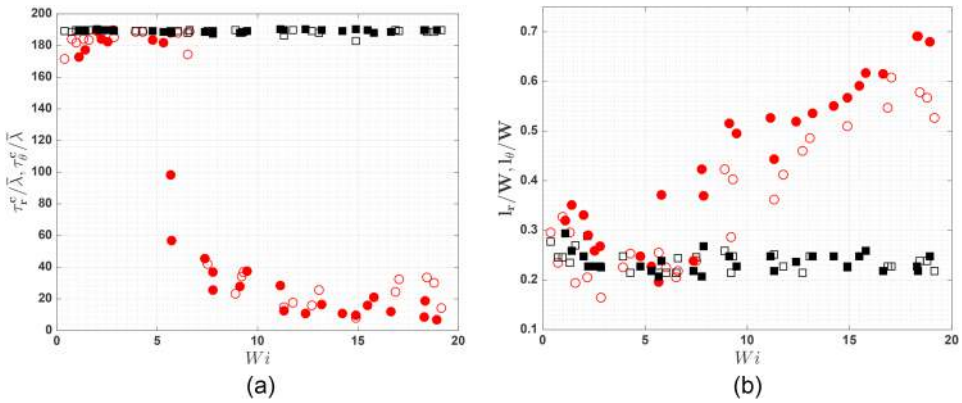

FIG. 20. (a) Correlation times of the fluctuations of the tangential (squares) and radial (circles) velocity components. (b) Correlation distances of the tangential (squares) and radial (circles) velocity components. The full/empty symbols refer to the increasing/decreasing branches of the controlled pressure ramp.

The measurements of the spatial correlations exemplified in Fig. 18 allow one to estimate the transversal correlation lengths of each velocity component as $\delta\xi_c^i = \frac{l_i}{W} = \frac{\int_0^1 |\xi C_{U_i}(\xi)| d\xi}{\int_0^1 |C_{U_i}(\xi)| d\xi}$, where $i = \theta, r$.

The dependencies of the normalised transversal correlation lengths $\frac{l_i}{W}$ of each velocity component on the global Weissenberg number are illustrated in Fig. 20(b). The correlation distance of the tangential velocity component is independent of *Wi* and accounts for roughly 25% of the width of the channel (the squares). Above the onset of elastic turbulence, the correlation distance of the radial component increases monotonically with *Wi* (the circles). In a fully developed turbulent regime, the transversal correlation length of the radial velocity component accounts for roughly 55% of the width of the channel, which is a quantitative proof of the smoothness of the flow field.

D. Statistical distributions of the velocity components, flow accelerations, structure functions, and power spectra

We focus in the following on the statistical distributions of the fluctuations of each velocity components and of the flow accelerations $\frac{dU(t)}{dt}$ as a function of both the reduced radial coordinate (within the bulk of the flow and at the edge of the boundary layers) and the global Weissenberg number as well as on the spectra of the velocity fluctuations.

The probability distribution functions (pdf's) of the fluctuations of both the tangential and the radial components of the velocity measured at the centre line of the micro-channel are presented in Fig. 21. Note that the fluctuations are scaled by their rms. Right above the onset of the primary elastic instability (the squares, the down triangles, and the rhombs in Fig. 21), the probability distributions are double peaked. This is due to the strong intermittency of the velocity signals and the emergence of rare events (see Fig. 10).

In a fully developed elastic turbulent regime, the probability distributions of each velocity component may be well described by a Gaussian function with very little skewness. This result is consistent with the measurements performed by Groisman and Steinberg in a macroscopic serpentine channel by means of Laser Doppler Velocimetry (LDV).[23]

Figure 22 shows the probability distributions of the normalised Eulerian accelerations of each velocity component $Y_i = \frac{1}{\langle U_i \rangle_t} \frac{dU_i(t)}{dt}$, $i = \theta, r$. The data were collected at the centre line of the micro-channel. We note that, corresponding to each velocity component, data collected for several global Weissenberg numbers collapse onto a single curve remarkably well, which is a signature of a universal statistical behaviour. Moreover, the probability distributions exhibit exponential tails. This result is fully consistent with the measurements

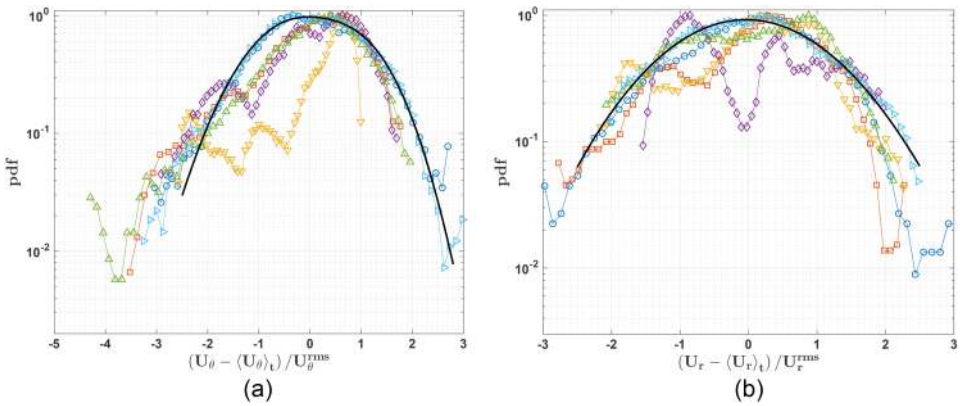

FIG. 21. (a) Probability distributions of the reduced fluctuations of the axial velocity measured at the centre line of the channel. The full line is a Gaussian fit. (b) Probability distributions of the reduced fluctuations of the radial velocity. The data were measured at the centre line of the channel. In both panels, the symbols refer to the driving pressures: blue circles–Δp = 1.9 kPa (*Wi* = 2.5), red squares–Δp = 5.1 kPa (*Wi* = 5.8), yellow down triangles–Δp = 8.3 kPa (*Wi* = 9.1), purple diamonds–Δp = 14 kPa (*Wi* = 14.2), green triangles–Δp = 20 kPa (*Wi* = 18.1), blue left triangles–Δp = 23 kPa (*Wi* = 18.3). The full lines are Gaussian fit functions.

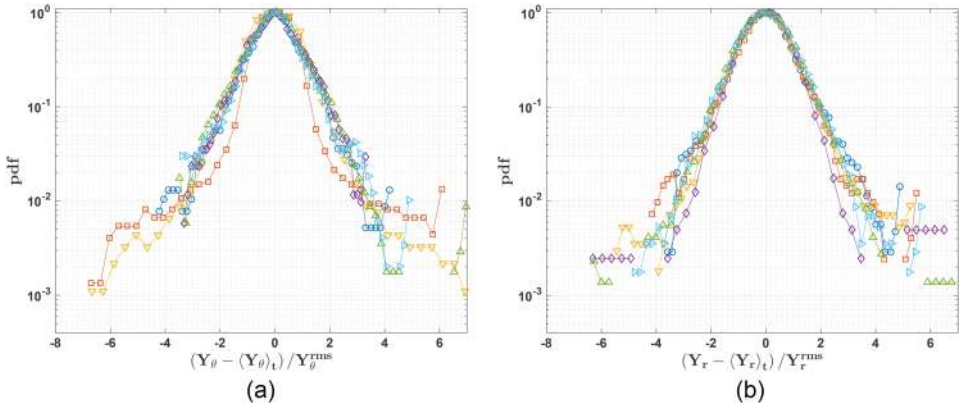

FIG. 22. (a) Probability distributions of the tangential acceleration. (b) Probability distributions of the radial acceleration. The data were measured at the centre line of the channel. The symbols refer to the driving pressures: blue circles–Δp = 5.1 kPa (Wi = 5.8), red square–Δp = 8.3 kPa (Wi = 9.1), yellow down triangles–Δp = 14 kPa (Wi = 14.2), purple diamonds–Δp = 20 kPa (Wi = 18.1), green triangles–Δp = 23 kPa (Wi = 18.3).

performed via Laser Doppler Velocimetry in a von Karman swirling flow.[14]

The power spectra of the fluctuations of the azimuthal velocity component measured at the midpoint of the channel ($\xi = 0$) for several Weissenberg numbers are presented in Fig. 23. In a laminar regime at $Wi = 1.1$, the spectrum is rather flat and solely reflects the level of instrumental noise of the measurements (the data labelled by a circle), which we have fully documented in Sec. III E. Within a fully developed elastic turbulent regime, a power law decay of the spectra is observed covering nearly four decades of magnitude in the power (the data labelled by up/down triangles and the rhombus), $P \propto f^{-\delta}$ with $\delta \approx 3.5$. The frequency range accounts for slightly more than a decade and the plateau is solely due to the presence of instrumental noise—unlike in the case of the inertial turbulence, here there exists no physical cut-off of the spectrum. A direct comparison with the theoretical prediction for the algebraic decay of the spectrum discussed in Sec. II requires the conversion of the spectra from the frequency to wave number domain. This conversion is typically done using the Taylor frozen flow hypothesis.[41] For the case of elastic turbulence it has been shown that in the presence

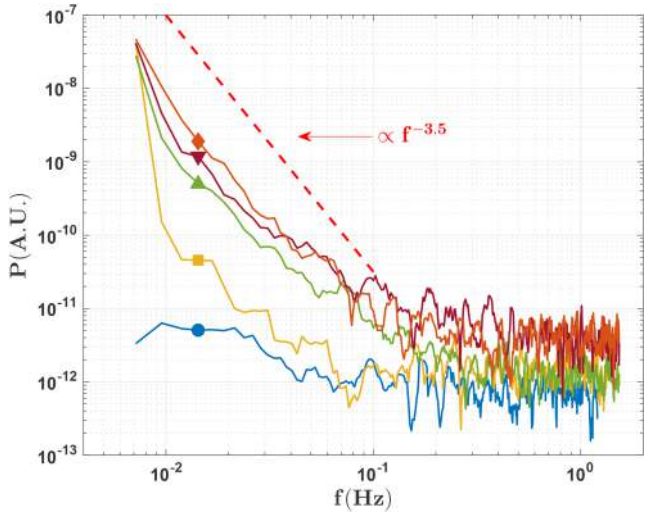

FIG. 23. Spectra of the fluctuations of the azimuthal velocity component measured at different Weissenberg numbers: blue circle–Δp = 0.9 kPa (Wi = 1.1), yellow square–Δp = 5.7 kPa (Wi = 7.3), green triangle–Δp = 7.6 kPa (Wi = 9.5), red down triangle–Δp = 10.2 kPa (Wi = 11.3), orange diamond–Δp = 23 kPa (Wi = 18.3).

of a strong mean flow, the Taylor hypothesis is applicable.[12] Thus, according to Lumley,[30] the spatial domain spectrum may be related to the frequency domain spectrum by:

$$P(k) = \langle U_i \rangle_t P(f) - \frac{I_t^2}{2} \frac{d^2 \left[k^2 P(k)\right]}{dk^2} + O(I_t^4), i = \theta, r, \quad (20)$$

where $I_t = \frac{U_i^{rms}}{\langle U_i \rangle_t}$ is the turbulence intensity associated with each velocity component. According to Eq. (20) if $P(f) \propto f^{-\delta_f}$ and $P(k) \propto k^{-\delta_k}$, the difference between the scaling exponents may be estimated as follows:

$$\delta_k - \delta_f \approx \frac{\log\left[1 + \frac{I_t^2}{2}\delta_k(2+\delta_k)\right]}{\log k}. \quad (21)$$

As in a regime of elastic turbulence the flow is smooth, a dominant wave number can be estimated using the size W of the micro-channel as $k \approx 3000\ \mathrm{m}^{-1}$. In the presence of a strong mean flow, which is the case here, for the tangential velocity component, the equation above leads to $\left|\delta_k - \delta_f\right| \ll 1$, which indicates that the decay exponent found experimentally in the frequency domain $\delta \approx 3.5$ can be meaningfully compared with the theoretical prediction given by Eq. (10). To conclude, the theoretical prediction of a spectral decay steeper than k^{-3} is verified.

We now focus on the statistics of the spatial increments of the second invariant of the rate of strain $\delta\dot{\underline{\underline{\gamma}}} = \dot{\underline{\underline{\gamma}}}(r + \delta r) - \dot{\underline{\underline{\gamma}}}(r)$ in a wide range of spatial increments from 2 μm to 66 μm measured at Wi = 18.3, Fig. 24. The spatial increments are normalised by the rms of the fluctuations of the second invariant. The probability distribution functions are fairly symmetric (though a slight right-sided skewness is visible) and have a Gaussian central part and exponential tails. Quite importantly, all the pdf's collapse onto a single curve, which is a signature of the scale invariance of the fluctuations of the velocity gradients.

An alternative way of assessing the statistical and scaling properties of elastic turbulence is to focus on the structure functions of the spatial increments of the second invariant of the rate of strain defined by:

$$S_{2p}(\frac{\delta r}{W}) = \left\langle \left| \dot{\underline{\underline{\gamma}}}\left[(\delta r + r_0)/W\right] - \dot{\underline{\underline{\gamma}}}(\delta r/W) \right|^{2p} \right\rangle_{r_0,t}. \quad (22)$$

Here the brackets $\langle . \rangle_{r_0,t}$ stand for the average over all various positions r_0 and the time. The high spatial resolution of the

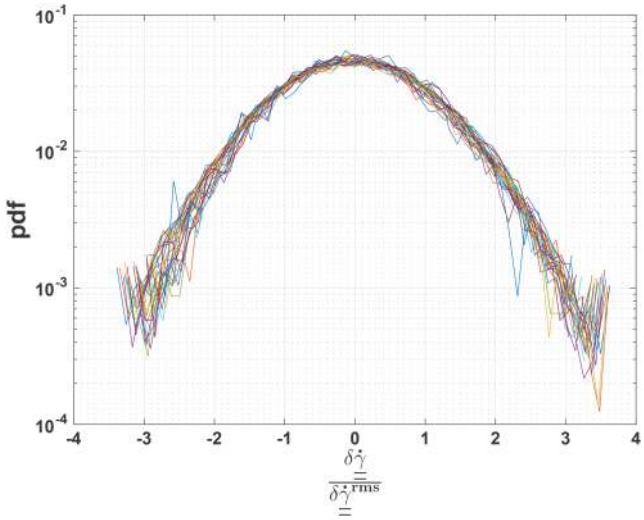

FIG. 24. Probability distribution function of the spatial velocity increments of the second invariant of the rate of deformation (see text for definition) measured at $Wi = 18.3$.

DPIV data together with a large size of the statistical ensemble (the series of velocity fields is acquired during a total time roughly 300 times larger than the polymer relaxation time) allows a reliable calculation of the structure functions up to the order 12.

Several second order structure functions of $\dot{\bar{\bar{\gamma}}}$ calculated for several Weissenberg numbers are exemplified in Fig. 25. As for the case of the inertial turbulence, we look for a scaling of the structure functions in the spatial range corresponding to the algebraic decay of the power spectrum in the form $S_{2p} \propto \left(\frac{\delta r}{W}\right)^{\xi_{2p}}$. The down-turn of the structure functions visible around $\delta r/W \approx 0.9$ is related to the presence of the elastic stress boundary layer. The power law scaling is observed in the range $\frac{\delta r}{W} \in [0.02\ 0.05]$.

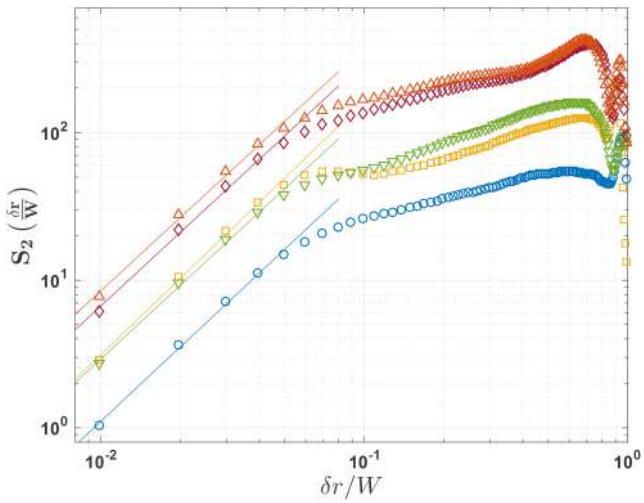

FIG. 25. Second order structure functions S_2 of the transversal increments of the second invariant of the rate of strain measured at several driving pressures: blue circles–$\Delta p = 5.1$ kPa ($Wi = 5.8$), yellow squares–$\Delta p = 8.3$ kPa ($Wi = 9.1$), orange triangles–$\Delta p = 14$ kPa ($Wi = 14.2$), red diamonds–$\Delta p = 20$ kPa ($Wi = 18.1$), green triangles–$\Delta p = 23$ kPa ($Wi = 18.3$).

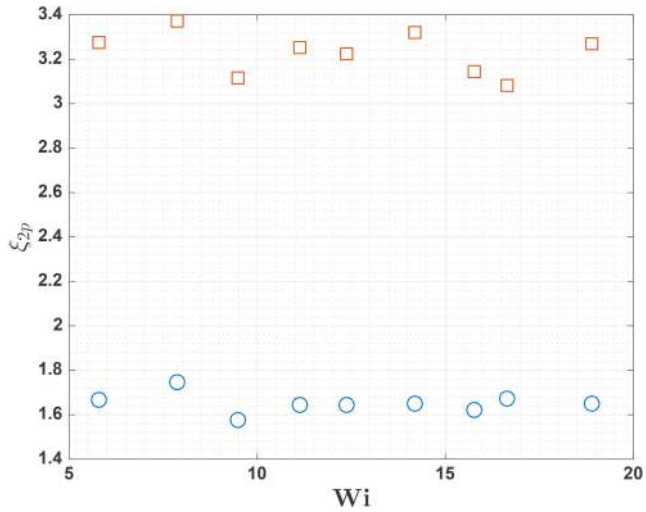

FIG. 26. Dependence of the scaling exponents ξ_2 (circles) and ξ_4 (squares) on the Weissenberg number.

The Weissenberg dependence of the scaling exponents of the second and fourth order structure functions is presented in Fig. 26. One can note that the scaling exponents ξ_2 and ξ_4 are independent of Wi over the entire range of elastic turbulence.

We focus now on the dependence of the scaling exponents on the order of the structure functions at various Wi. For this purpose, we illustrate structure functions up to order 12 (only the even orders are shown) computed for the highest Wi explored in our experiments ($Wi = 18.3$), Fig. 27. We have checked that the calculation of structure functions of orders higher than 12 was unreliable.

The dependence of the scaling exponents ξ_{2p} on the order of the structure functions obtained for several Wi is illustrated in Fig. 28. In a fully developed elastic turbulent regime, a linear dependence is observed $\xi_{2p} = 0.009\,598(\pm 10^{-4}) + 0.816(\pm 0.04)\,(2p)$ (the full line). This behaviour is substantially different from the passive scalar behaviour,[24]

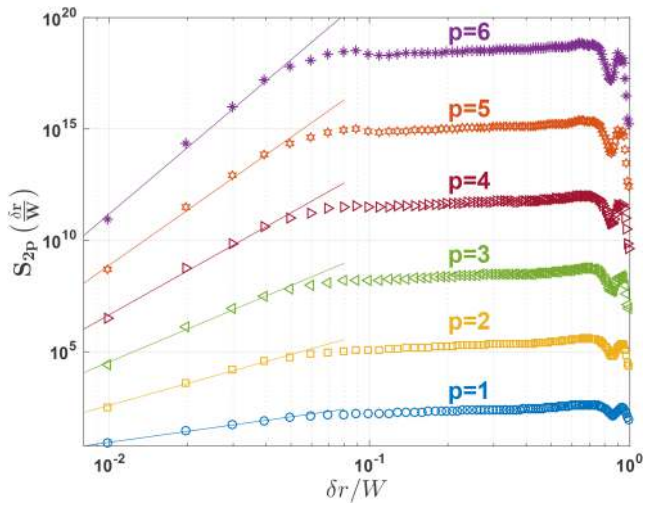

FIG. 27. Structure functions S_{2p} of the transversal increments of the second invariant of the rate of strain measured at $Wi = 18.3$. The full lines are power law fit functions $S_{2p} \propto \left(\frac{\delta r}{W}\right)^{\xi_{2p}}$.

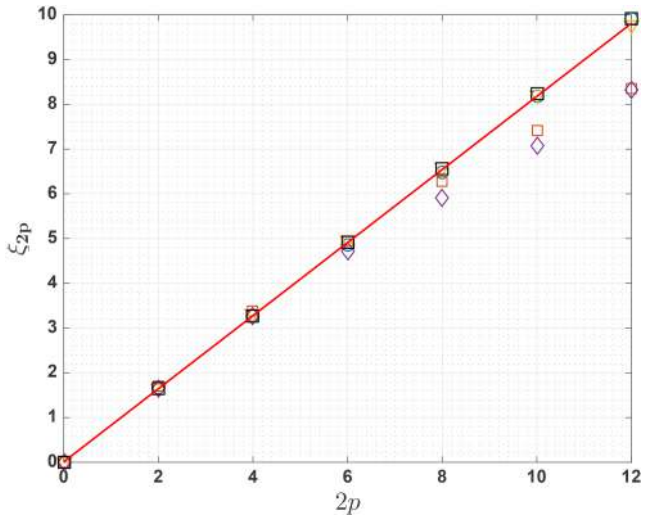

FIG. 28. Scaling exponents of the even order structure functions for several driving pressures: blue circles–Δp = 5.1 kPa (Wi = 5.8), orange squares–Δp = 8.3 kPa (Wi = 9.1), yellow down triangles–Δp = 14 kPa (Wi = 14.2), purple diamonds–Δp = 20 kPa (Wi = 18.1), green triangle–Δp = 23 kPa (Wi = 18.3). The full line is a linear fit $\xi_{2p} = 0.009\,598(\pm 10^{-4}) + 0.816(\pm 0.04)$ $(2p)$.

but consistent with the form of the pdf's presented in Fig. 24.

V. CONCLUSIONS AND OUTLOOK

A systematic experimental investigation of the flow of a dilute polymer solution in a curvilinear micro-channel has been presented for a broad range of Weissenberg numbers. A custom developed *DPIV* technique allowed one to characterise both the spatial structure and the long time statistics of flow fields. Let us summarise the main findings of our study. All measured flow quantities are reproducible upon increasing/decreasing the global Wi, which demonstrates that the transition to elastic turbulence is a continuous one, Figs. 8, 13, 16, 17, and 20. Moreover, the dependence of the *rms* of fluctuations of each velocity component on the control parameter may be described by the stationary Landau-Ginzburg equation with a field that indicates that the transition to elastic turbulence emerges via a supercritical bifurcation, Fig. 13. This scenario is quite different from that observed in a Couette flow and still awaits a theoretical investigation. Measurements of time series of the flow fields during total times roughly 300 times longer than the average relaxation time of polymer molecules reveal a strong flow intermittency manifested through the emergence of rare flight-crash events right above the onset, Fig. 11. The dependencies of both the time averaged and *rms* of the fluctuations of the second invariant of the rate of strain tensor on the reduced transversal coordinate exhibit two distinct peaks in the vicinity of the channel's boundaries Figs. 14 and 15. Such peaks have been previously observed during experiments performed in a von Karman swirling flow between disks[7,14] and can be associated with the emergence of an elastic stress boundary layer. In a fully developed elastic turbulent regime, the width of the boundary layer is independent of the global Wi number and accounts for roughly 10% of the channel's width Fig. 16. The strongly inhomogeneous spatial distribution of velocity gradients hints at a plausible physical interpretation for the emergence of rare events in terms of an accumulation of the elastic stresses in the boundary layers and their intermittent re-injection into the flow. A similar intermittent scenario has been observed during the mixing of a passive scalar in a micro-channel.[8]

An important finding of our study concerns with the evolution of the local Weissenberg number Wi_{loc} with the global Weissenberg number: Wi_{loc} increases at the peaks of the elastic stress boundary layers but remains roughly constant in the bulk of the flow, Fig. 17(b). Thus, the main assumptions of the theory of elastic turbulence are qualitatively validated. Quantitatively, however, the saturation value is roughly 15.5 times larger than the unitary value predicted by the theory. This quantitative discrepancy might be related to the presence of the elastic stress boundary layers with widths of the same order of magnitude as the size of the micro-channel. Measurements of both the spatial and temporal correlations of each velocity component (Figs. 18 and 19) allowed one to calculate the corresponding correlation distances and times. Whereas the fluctuations of the tangential velocity component are long-time correlated regardless of the value of Wi, the correlation time of the radial component decreases with Wi and saturates at a value roughly equal to 13 times the average relaxation time, Fig. 20(a). This result disagrees with both previous measurements performed in a macroscopic von Karman swirling flow[7,14] and the theory that predicts a value comparable to the average relaxation time. Once again we attribute this discrepancy to the presence of a thick elastic stress boundary layer. The fluctuations of the tangential velocity component are strongly correlated along the transversal flow direction, and the correlation length is independent of the control parameter—the squares in Fig. 20. As Wi is increased, the correlation length of the fluctuations of the radial velocity component increases and then saturates at a value accounting roughly for half channel width—the circles in Fig. 20.

The time-resolved *DPIV* technique allowed one to acquire a statistically relevant amount of flow data and assess the probability distributions of the fluctuations of each velocity component, Fig. 21. Slightly above the onset of the transition, the pdf's are doubly peaked and exhibit a strong left-side skewness. This is related to the strong intermittency of the flow and the emergence of the rare events. In a fully developed elastic turbulent regime, the pdf's have a nearly Gaussian shape. The pdf's of both components of the flow accelerations measured at the centre-line of the micro-channel are symmetric and exhibit exponential tails, Fig. 22. In agreement with both the theoretical prediction and the measurements performed in macroscopic flows, the spectra of the velocity fluctuations decay algebraically and the decay exponent satisfies the condition $\delta \geq 3$, Fig. 23. The pdf's of the spatial increments of the second invariant of the normalised rate of deformation collapse onto a single curve with a Gaussian central part and exponential tails, Fig. 24. This is a signature of the scale invariance of the velocity gradients in a regime of fully developed elastic turbulence.

The structure functions of the second invariant of the rate of strain scale algebraically within a range of distances

$\delta r/W < 0.05$, Figs. 25 and 27 and the scaling exponents are independent of the Weissenberg number, Fig. 26.

In closing, we highlight several issues that still need to be addressed by future theoretical studies. First, the continuous and reversible nature of the bifurcation towards elastic turbulent flow states needs to be explained. Second, new theoretical insights are needed to understand the emergence of the elastic stress boundary layer and its physical properties, notably the invariance of its width with the control parameter. Third, the quantitative disagreement on the saturation of the velocity gradients in a regime of elastic turbulence needs to be addressed most probably in connection to the emergence of the elastic stress boundary layer.

ACKNOWLEDGMENTS

We thank Gwenaël Biotteau for designing and machining the micro-channel. We gratefully acknowledge the financial support from the Agence Nationale de la Recherche (ANR) via Project No. HoTeT (*ANR*–13–*JS*09–0012).

[1] Abed, W. M., Whalley, R. D., Dennis, D. J., and Poole, R. J., "Numerical and experimental investigation of heat transfer and fluid flow characteristics in a micro-scale serpentine channel," Int. J. Heat Mass Transfer **88**, 790–802 (2015).
[2] Balkovsky, E., Fouxon, A., and Lebedev, V., "Turbulence of polymer solutions," Phys. Rev. E **64**, 056301 (2001).
[3] Barnes, H. A., Hutton, J. F., and Walters, K., *An Introduction to Rheology*, Rheology Series, 1st ed. (Elsevier Science, 1989).
[4] Batchelor, G. K., "Small-scale variation of convected quantities like temperature in turbulent fluid. Part 1. General discussion and the case of small conductivity," J. Fluid Mech. **5**(1), 113 (1959).
[5] Bazilevskii, A. V., Entov, V. M., Lerner, M. M., and Rozhkov, A. N., "Failure of polymer solutions filaments," Polym. Sci., Ser. A **39**, 316–324 (1997).
[6] Bird, B. R. and Hassager, O., *Dynamics of Polymeric Liquids: Fluid Mechanics*, Dynamics of Polymer Liquids Vol. 1, 2nd ed. (Wiley-Interscience, 1987).
[7] Burghelea, T., "Elastic turbulence and mixing in a dilute polymer solution," Ph.D. thesis, Feinberg Graduate School of the Weizmann Institute of Science, 2005.
[8] Burghelea, T., Segre, E., Bar-Joseph, I., Groisman, A., and Steinberg, V., "Chaotic flow and efficient mixing in a microchannel with a polymer solution," Phys. Rev. E **69**(6), 066305–066308 (2004).
[9] Burghelea, T., Segre, E., and Steinberg, V., "Mixing by polymers: Experimental test of decay regime of mixing," Phys. Rev. Lett. **92**(16), 164501–164504 (2004).
[10] Burghelea, T., Segre, E., and Steinberg, V., "Statistics of particle pair separations in the elastic turbulent flow of a dilute polymer solution," Europhys. Lett. **68**(4), 529 (2004), URL: http://stacks.iop.org/0295-5075/68/i=4/a=529.
[11] Burghelea, T., Segre, E., and Steinberg, V., "Elastic turbulence in von Karman swirling flow between two disks," Phys. Fluids **19**(5), 053104 (2007).
[12] Burghelea, T., Segre, E., and Steinberg, V., "Validity of Taylor hypothesis in a random spatially smooth flow," Phys. Fluids **17**(10), 103101–103108 (2005).
[13] Burghelea, T., Segre, E., and Steinberg, V., "Role of elastic stress in statistical and scaling properties of elastic turbulence," Phys. Rev. Lett. **96**(21), 214502–214504 (2006).
[14] Burghelea, T., Segre, E., and Steinberg, V., "Elastic turbulence in von Karman swirling flow between two disks," Phys. Fluids **19**(5), 053104 (2007).
[15] Chertkov, M., "On how a joint interaction of two innocent partners (smooth advection and linear damping) produces a strong intermittency," Phys. Fluids **10**(11), 3017–3019 (1998).
[16] Doi, M. and Edwards, S. F., *The Theory of Polymer Dynamics* (Clarendon Press, Oxford, 1986).
[17] Entov, V. and Hinch, E., "Effect of a spectrum of relaxation times on the capillary thinning of a filament of elastic liquid," J. Non-Newtonian Fluid Mech. **72**(1), 31–53 (1997).
[18] Fetecau, C. and Fetecau, C., "Unsteady flows of Oldroyd-B fluids in a channel of rectangular cross-section," Int. J. Non-Linear Mech. **40**(9), 1214–1219 (2005).
[19] Fouxon, A. and Lebedev, V., "Spectra of turbulence in dilute polymer solutions," Phys. Fluids **15**(7), 2060–2072 (2003).
[20] Groisman, A. and Steinberg, V., "Mechanism of elastic instability in Couette flow of polymer solutions: Experiment," Phys. Fluids **10**(10), 2451–2463 (1998).
[21] Groisman, A. and Steinberg, V., "Elastic turbulence in a polymer solution flow," Nature **405**(6782), 53–55 (2000).
[22] Groisman, A. and Steinberg, V., "Efficient mixing at low Reynolds numbers using polymer additives," Nature **410**(6831), 905–908 (2001).
[23] Groisman, A. and Steinberg, V., "Elastic turbulence in curvilinear flows of polymer solutions," New J. Phys. **6**(1), 29 (2004).
[24] Jun, Y. and Steinberg, V., "Mixing of passive tracers in the decay Batchelor regime of a channel flow," Phys. Fluids **22**(12), 123101 (2010).
[25] Jun, Y. and Steinberg, V., "Elastic turbulence in a curvilinear channel flow," Phys. Rev. E **84**, 056325 (2011).
[26] Kulicke, W. M., Kotter, M., and Grager, H., *Polymer Characterization/Polymer Solutions*, Advances in Polymer Science Vol. 89 (Springer-Verlag, Berlin, 1989).
[27] Larson, R. G., "Instabilities in viscoelastic flows," Rheol. Acta **31**(3), 213–263 (1992).
[28] Li, D.-Y., Li, X.-B., Zhang, H.-N., Li, F.-C., Qian, S., and Joo, S. W., "Efficient heat transfer enhancement by elastic turbulence with polymer solution in a curved microchannel," Microfluid. Nanofluid. **21**(1), 10 (2017).
[29] Liu, Y. and Steinberg, V., "Molecular sensor of elastic stress in a random flow," Europhys. Lett. **90**(4), 44002 (2010), URL: http://stacks.iop.org/0295-5075/90/i=4/a=44002.
[30] Lumley, G. L. and Lumley, J. L., "On the solution of equations describing small scale deformation," Symp. Math. **9**, 315–334 (1972).
[31] McKinley, G. H., Pakdel, P., and Öztekin, A., "Rheological and geometric scaling of purely elastic flow instabilities," J. Non-Newtonian Fluid Mech. **67**, 19–47 (1996).
[32] Morozov, A. N. and van Saarloos, W., "An introductory essay on subcritical instabilities and the transition to turbulence in visco-elastic parallel shear flows," Phys. Rep. **447**(3–6), 112–143 (2007); Casademunt, J., "Nonequilibrium physics: From complex fluids to biological systems I. Instabilities and pattern formation," *ibid.* **447**, 67 (2007).
[33] Muller, S. J., Larson, R. G., and Shaqfeh, E. S. G., "A purely elastic transition in Taylor-Couette flow," Rheol. Acta **28**(6), 499–503 (1989).
[34] Ogilvie, G. I. and Proctor, M. R. E., "On the relation between viscoelastic and magnetohydrodynamic flows and their instabilities," J. Fluid Mech. **476**, 389–409 (2003).
[35] Raffel, M., Willert, C. E., Wereley, S. T., and Kompenhans, J., *Particle Image Velocimetry: A Practical Guide*, Experimental Fluid Mechanics, 2nd ed. (Springer, 2007).
[36] Scarano, F. and Rhiethmuller, M. L., "Advances in iterative multigrid PIV image processing," Exp. Fluids **29**, S051 (2001).
[37] Schuberth, S., "Rheologische untersuchungen an polyisobutylenen und polyacrylamidlösungen mit einem neuartigen optischen dehnrheometer," Ph.D. thesis, Der Technischen Fakultat der Universität Erlangen-Nürnberg, 2008.
[38] Shaqfeh, E. S. G., "Purely elastic instabilities in viscometric flows," Annu. Rev. Fluid Mech. **28**(1), 129–185 (1996).
[39] Steinberg, V., "Elastic stresses in random flow of a dilute polymer solution and the turbulent drag reduction problem," C. R. Phys. **10**(8), 728–739 (2009).
[40] Sureshkumar, R., Beris, A. N., and Avgousti, M., "Non-axisymmetric subcritical bifurcations in viscoelastic Taylor-Couette flow," Proc. R. Soc. A **447**(1929), 135–153 (1994).
[41] Taylor, G. I., "The spectrum of turbulence," Proc. R. Soc. A **164**(919), 476–490 (1938).
[42] Traore, B., Castelain, C., and Burghelea, T., "Efficient heat transfer in a regime of elastic turbulence," J. Non-Newtonian Fluid Mech. **223**, 62–76 (2015).
[43] Wang, J., Huang, H., and Huang, X., "Molecular weight and the Mark-Houwink relation for ultra-high molecular weight charged polyacrylamide

determined using automatic batch mode multi-angle light scattering," J. Appl. Polym. Sci. **133**(31) (2016).
[44]Waters, N. D. and King, M. J., "Unsteady flow of an elastico-viscous liquid," Rheol. Acta **9**(3), 345–355 (1970).
[45]White, J. L. and Metzner, A. B., "Development of constitutive equations for polymeric melts and solutions," J. Appl. Polym. Sci. **7**(5), 1867–1889 (1963).
[46]Zilz, J., Poole, R. J., Alves, M. A., Bartolo, D., Levaché, B., and Lindner, A., "Geometric scaling of a purely elastic flow instability in serpentine channels," J. Fluid Mech. **712**, 203–218 (2012).
[47]Zimm, B. H., "Dynamics of polymer molecules in dilute solution: Viscoelasticity, flow birefringence and dielectric loss," J. Chem. Phys. **24**(2), 269–278 (1956).